5-1-2019

Numerical Study of Spacer Grid Geometry in a 5 X 5 Nuclear Fuel Rod Bundle

Wan Chuan Fan
jasonfanjf@hotmail.com

NUMERICAL STUDY OF SPACER GRID GEOMETRY IN A 5 X 5

NUCLEAR FUEL ROD BUNDLE

By

Wan Chuan Fan

Bachelor of Science in Engineering – Mechanical Engineering
University of Nevada, Las Vegas
2018

A thesis submitted in partial fulfillment
of the requirements for the

Master of Science in Engineering – Mechanical Engineering

Department of Mechanical Engineering
Howard R. Hughes College of Engineering
The Graduate College

University of Nevada, Las Vegas
May 2019

This thesis prepared by

Wan Chuan Fan

entitled

Numerical Study of Spacer Grid Geometry in a 5 X 5 Nuclear Fuel Rod Bundle

is approved in partial fulfillment of the requirements for the degree of

Master of Science in Engineering – Mechanical Engineering
Department of Mechanical Engineering

<table>
<tr><td>Yi-Tung Chen, Ph.D.
Examination Committee Chair</td><td>Kathryn Hausbeck Korgan, Ph.D.
Graduate College Dean</td></tr>
<tr><td>William Culbreth, Ph.D.
Examination Committee Member</td><td></td></tr>
<tr><td>Robert Boehm, Ph.D.
Examination Committee Member</td><td></td></tr>
<tr><td>Jichun Li, Ph.D.
Graduate College Faculty Representative</td><td></td></tr>
</table>

ABSTRACT

Numerical Study of Spacer Grid Geometry in a 5 x 5 Nuclear Fuel Rod Bundle

by

Wan Chuan Fan

Dr. Yi-Tung Chen, Examination Committee Chair
Professor, Department of Mechanical Engineering
University of Nevada, Las Vegas

Reactor fuel rod bundles serve as the primary heat source in light water reactors (LWRs), commonly found in the aforementioned PWR plants. The fuel rod bundles' structure consists of a collection of fuel rods put into a parallel grid configuration. The bundles also include fuel rod spacers, which hold the fuel rods in place, in accordance with the grid. Repeating structures of the fuel bundles create the meta-structure in the reactor. In other words, the grid configuration repeats until it fills the entire space of the reactor. This results in reactor fuel rods suspended in the working fluid domain, oriented parallel length-wise to the flow direction, by the spacer grids.

The generated heat from the fission reactions within the fuel rod elements provide the primary heat source for the power cycle. As the working fluid, light water, in this case, flows through the reactor, the heat generated by the fuel rods' fission reactions is transferred to the fluid, adding its potential to do work. Taking advantage buoyancy effects of the heated working fluid, reactors usually have the working fluid enter through the bottom, then pumped up vertically through the fuel rod bundles and spacers.

Since the working fluid flows through a flow region inside the reactor, containing fuel rod elements and the spacer grids, the drag force caused by these obstacles requires extra pumping power to overcome. This need for extra pumping power lowers total

thermal system efficiency. Fortunately, the spacers have extra geometries in the end called mixing vanes, which agitate the working fluid as it flows through the reactor, disturbing the hydraulic and thermal boundary layers. As these boundary layers are disturbed, heat transfer rate increases; which, in turn, increases the amount of energy added to the working fluid during the heat addition phase of the thermal power cycle, adding more potential to do work in the work output phase of the cycle.

Focusing only on hydraulic performances, this study attempted to lower hydraulic pressure drop across the spacer grid by numerically simulating spacer grids with different changes to their geometries inside a flow field. Several geometrical variations were chosen due to their ease of manufacturing and minimal tooling changes required at the supplier level; these variations include spacer grid length, mixing vane angle, spacer grid entrance geometry, and mixing vane shape.

This study used the sectional method proven by Conner et al. (2010) and Navarro et al. (2011), to establish its baseline. In order to save the limited resources in computational power, the results from Navarro et al. (2011) were first transferred from CFX to Fluent 18.2. This step required the numerical results from both software to be compared and benchmarked. Fluent's segregated method of calculating velocity and pressure makes the calculations easier on the limited hardware. In addition, Fluent's finite volume method with cell-centered scheme also allows solutions to more accurately reflect cases where unstructured meshes are used, such as this study. To justify the results, this study also introduced different fluid domain inlets, additional boundary layers, and finer mesh sizes than the previous studies that provided the baseline.

Mesh independent study was done to find the correct mesh size for a good compromise between resolution and convergence time. The results show that an element count of 4.27×10^7 or greater yielded computational results independent from element counts. However, since going with a higher element count does not significantly lengthen the computational time, the highest element count 6.18×10^7 elements, along with its respective body-sizing, 3.0×10^{-4} m, were chosen. The resulting y+ values of this study was around 1.75, less than the value used by Navarro et al. (2011). The total pressure drop across the region of interest also closely replicated the previous results found by various studies.

Lastly, the study compared results from each variation. Shortening the spacer grid length decreases the pressure drop across its span. However, with a 25% reduction in spacer grid length, the pressure drop only reduced by 10.2%. This implied that the reduction in spacer grid length does not scale in unity with the reduction in pressure drop. Fortunately, increasing mixing vane angle significantly increase the agitation of the boundary layers. Specifically, a 20% increase in the mixing vane angle resulted in a 15.6% increase in swirl-factor, with only around 9.28% increase in pressure drop. Meanwhile, adding a 45-degree chamfer to the entrance of the spacer grid, with depth that bisects its thickness, decreased the pressure drop by 47%, without adding significant manufacturing steps to the construction. Then, a curvature was added to the mixing vane's profile to ease fluid flow's transition back to the freestream. However, the curvature on the mixing vane had detrimental effects on the overall performance, increasing the pressure drop across the spacer by 31.3%, while decreasing swirl factor by 4.3%.

TABLE OF CONTENTS

LIST OF FIGURES

LIST OF NOMENCLATURE

Alphabets

- C – Constant term (unit depends on context)
- C_f – Coefficient of friction (dimensionless)
- k – Turbulent kinect energy $(\frac{m^2}{s^2})$
- l – Length of the spacer grid, excluding mixing vane (m)
- L – Length of the fluid domain (m)
- p – Pressure (Pa)
- P – Production rate term $(\frac{m^2}{s^3})$
- Q_{in} – Heat input to the power cycle (kJ)
- Re – Reynolds number (dimensionless)
- Δs – First layer thickness (m)
- S – Strain rate (dimensionless)
- SF – Swirl Factor (dimensionless)
- t – Time (s)
- u_i – Velocity $(\frac{m}{s})$
- U_∞ - Freestream velocity $(\frac{m}{s})$

Greeks

- ε – Dissipation rate $(\frac{m^2}{s^3})$
- η_{th} - Thermal effciency (%)
- μ – Dynamic viscosity $(Pa * s)$
- ρ – Density $(\frac{kg}{m^3})$
- τ – Shear stress (Pa)

CHAPTER 1 BACKGROUND AND OBJECTIVES

1.1. Introduction

Pressurized water reactor (PWR)-based power plants, shown in Figure 1, depend on pressurized reactor cores for their heat addition phase. The heat generated by the fission reaction of the fuel rod elements transfer to the working fluid inside these reactor cores. The pressure inside the reactor cores prevents the working fluid from entering the boiling regime, which wastes thermal energy in the form of latent heat, without creating a higher temperature difference in order to do work. These reactor cores contain solid fission fuel elements in the shape of thin, long, rods, which are suspended vertically inside the fluid domain by the spacer grids, parallel to the flow direction. This allows the working fluid, in this case, light water, to flow through the reactor from bottom to top, taking advantage of buoyancy effects during heating, as the density of water decreases over the heat addition phase. Taking advantage of the buoyancy effect reduces the pumping power required for the fluid to go through the reactor core, decreasing the overall parasitic loads of the thermal power cycle. Upon leaving the reactor core, the now heated primary working fluid enters a heat exchanger (HX) and transfers the heat gathered in the reactor core to the secondary coolant. Then, the secondary coolant enters the turbine and enters the work extraction phase of the thermal cycle. After leaving the HX, the primary working fluid gets pumped back into the reactor core, completing the primary loop of the power plant.
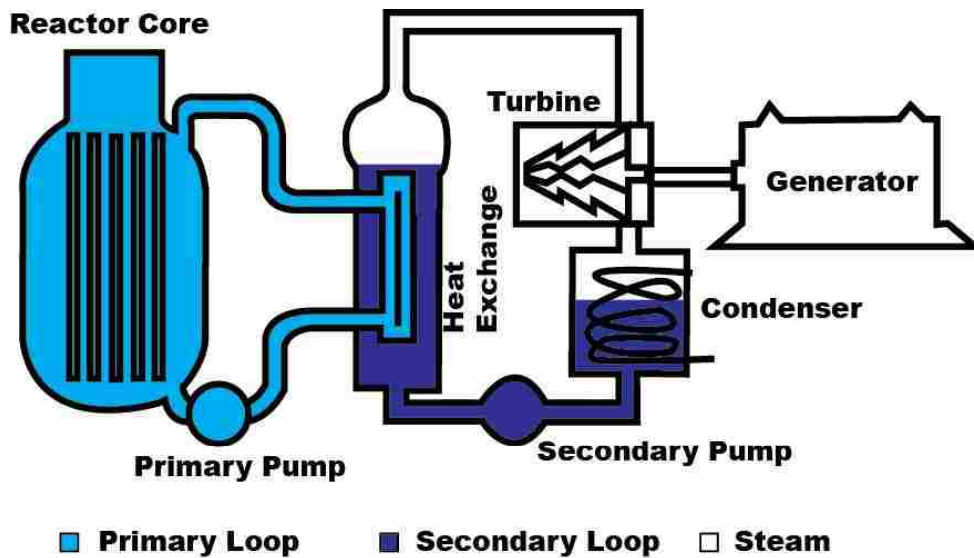
Figure 1 A simple diagram of a PWR power plant

Since the secondary working fluid acquires heat from the primary working fluid in the HX, the temperature difference between the two determines the amount of heat transferred to the secondary working fluid. This further explains why the primary working fluid is kept from boiling while attempting to gather more heat from the heat addition phase inside the reactor. Additionally, if boiling were to happen inside the primary loop, vapor voids would appear, which act as extra thermal resistance in the heat transfer process between the fuel rod elements and the working fluid itself. This reduction in heat transfer rate also increases the amount of heat stored inside the fuel rod elements, which increases the chance of a reactor core meltdown.

As mentioned previously, the spacer grids inside the reactor core holds the fuel rod elements in place to maintain the grid layout meta-structure while also preventing unwanted vibrations across the fuel rod element's length due to being suspended inside the flow field of the working fluid. The added mixing vanes downstream also serves to agitate the fluid flow around the fuel rods, encouraging flow in directions other than

axial. The agitation breaks the hydraulic and thermal boundary layers to increase the heat

transfer rate, while further preventing overheating of the fuel rod elements.

Unfortunately, the spacer grids' functions come at a cost. The extra obstacle

created by the spacer grids inside the flow field causes increased pressure drop due to the

extra drag forces. The increased pressure drop, in turn, requires more pumping power to

overcome. As Equation (1) describes, the overall thermal efficiency of a power plant,

η_{th}, is dependent on the heat added to the thermal cycle, Q_{in}, the work output from the

turbine, W_T, and the work input to the pump, W_P.

$$\eta_{th} = \frac{W_T - W_P}{Q_{in}} \qquad (1)$$

Thus, given the same turbine output from the secondary loop, lowering the

required work input to the pump in the primary loop improves the efficiency of the power

plant. Additionally, heat transfer to the secondary working fluid increases when a higher

temperature difference can be maintained between the primary and secondary working

fluids when they are inside the HX. As a result, the increase in gathered thermal energy

from the primary working fluid increases the extractable work from the secondary

working fluid during the work output stage at the turbine.

The sum of the above factors shows the significant impact pressure drop inside

the reactor core has on the whole power plant. Therefore, by reducing the input required

at the pump, while adding the agitation, which increases heat transfer rate in the reactor

core, should cause a dramatic improvement in the overall thermal efficiency of the power

plant. Likewise, studying the main factors causing the hydraulic pressure drop and

agitation across the spacer grids helps achieve that goal. This study focuses on the geometrical factors that are easy to manipulate in a manufacturing environment but present significant impact on the flow characteristics. Figure 2 shows the structure of a PWR reactor core and the spacer grid within. Figure 3 focuses on the spacer grid, showing the two primary components of a spacer grid, which include the spacer grid subchannels which hold the fuel rod elements in place and the mixing vanes downstream to cause agitation in the fluid flow.

Although crucial, experimental studies involving fluid mechanics in the scale that is required to fully understand the impact of various geometrical changes are expensive to conduct due to the cost to manufacture the various spacer grids corresponding to each variation and to acquire the necessary sensors. In addition, the time investment required to setup each case for study presents another layer of cost. As a result, finding the proper numerical models for fluid flow simulation became of increasing importance in the field of fluid mechanics. Current advancements in available commercial numerical simulation software and computer hardware have allowed computational fluid dynamics (CFD) to become a more widespread and viable way of predicting the fluid behavior in a given computational domain.
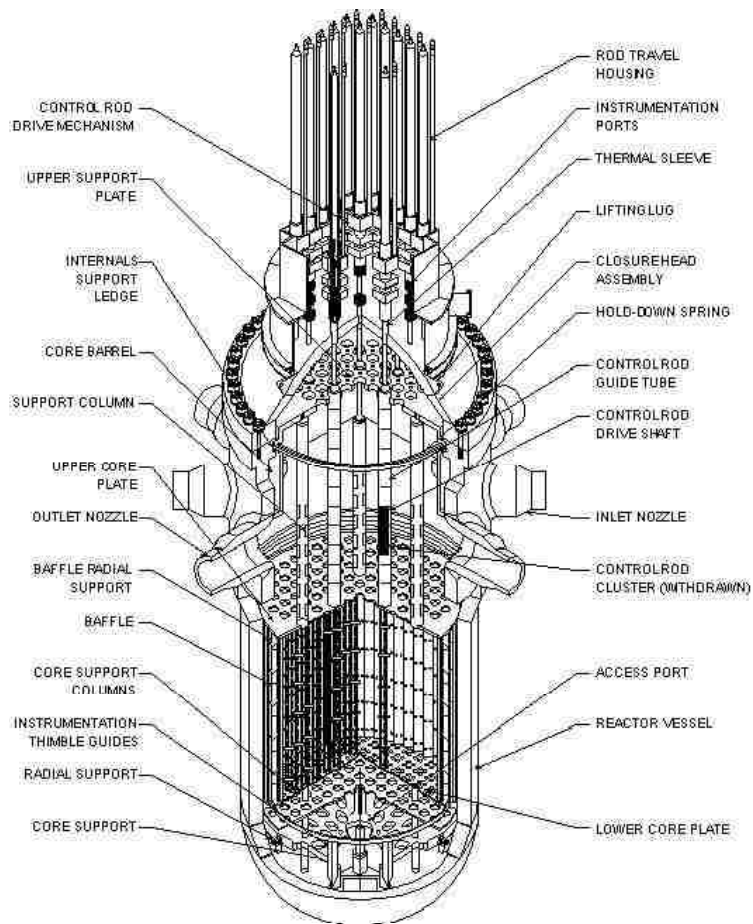
Figure 2 Cut away view of a pressurized water reactor core, showing the overview of major components
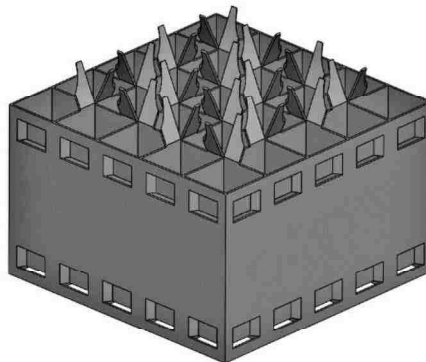
Figure 3 An isometric view of a 5 x 5 spacer grid and mixing vanes

1.2. Literature survey

1.2.1. Previous Studies

Literature survey for this study included the ASME database, the UNLV library database and Google Scholar. These search inquiries cover journal indexes which include databases from *International Heat and Mass Transfer* and *American Nuclear Society*.

Fluid mechanic engineers have tried to develop ways to mathematically correlate the various fluid flow characteristics to the geometrical characteristics of the fluid domain. Rehme (1973) developed simple mathematical correlations for pressure drop across a nuclear spacer geometry. He discovered blockage ratio, length, and hydraulic diameter being the primary variables in pressure drop across the length of the bundle. He then proceeded to create a simple algebraic analytical mathematical correlation to predict the pressure drop across the reactor spacer grid with the aforementioned variables.

Yao et al. (1982) studied the effects of the spacer bundles on heat-transfer, without the aid of CFD. They proposed a new prediction model for critical heat flux and suggested slight altercations to Rehme's (1973) analytical prediction for pressure drop. Additionally, Yao et al. (1982) also provided the first experimental pressure drop correlations on simple spacer grid geometries without mixing vanes using a modified version of Rehme's (1973) method.

Conner et al. (2010) performed a CFD simulation of a simplified fluid domain, using a sectional method. By cutting the domain into sections, the computational time was shortened and the hardware limitations of the time were negated. When compared to with experimental results gathered by Smith et al. (2002), the results in Conner et al.

(2010) were highly accurate in their study. The sectioning methods proven by Conner et al. (2010) formed the basis of the methodology used in the present study.

Navarro et al. (2011) further successfully simulated the flow inside a 5 x 5 PWR reactor fuel rod bundle using an available commercial software package, ANSYS-CFX. The total pressure drop obtained by Navarro et al. (2011) were close to previously obtained results from Chun and Oh (1998). Additionally, Navarro et al. (2009) also utilized the domain sectioning method in their study.

Liu et al. (2012) compared different turbulence models for their performances in a PWR spacer grid. They concluded that the $k - \omega$ SST and the realizable $k - \varepsilon$ turbulence models worked the best, depending on the Reynolds number. However, Chen et al. (2016) proved that the RNG $k - \varepsilon$ turbulence model also works reasonably well with faster computing times. Finally, Cheng et al. (2016) simulated 5 x 5 fuel rod bundle and stacked spacer grids. Cheng et al. (2016) proved the improvement in computing hardware by calculating a large fluid domain containing multiple smaller fluid domains that were previously too difficult to simulate.

1.2.2. Numerical Methods and Fluid Specific Survey

The main governing equations found in the ANSYS Fluent manual (ANSYS, Inc. 2009) traces its root from fluid mechanic textbooks such as White's (2006). Meanwhile, nuances within the numerical simulation came from fluid mechanic textbooks with more in-depth chapter on computational fluid dynamics (White, 2003). Additionally, Versteeg and Malalasekera (2007) covered the finite volume method (FVM) extensively, which embodies the solution methods for the numerical modeling in this study.

1.2.3. Research Objective

This study focuses only on the hydraulic effects of various spacer grid geometries that do not require a significant investment in capital, time, or tooling to alter. The geometries include spacer grid subchannel length, mixing vane angle, spacer grid entrance chamfer, and mixing vane shape. Lowering the pressure drop across the length of the spacer represents the top priority. Meanwhile, increasing the agitation in the fluid flow, measured as the ratio between axial and non-axial velocity magnitudes, is maximized without significantly increasing pressure drop.

1.3. Motivation for Study

Nuclear power accounts for 60% of total non-greenhouse-gas-emitting electric sources (the Office of Nuclear Energy of the Department of Energy, 2019) in the United States, which amounts to about 20% of total power consumed. Additionally, this number is projected to grow by 1%, annually (the U.S. Energy Information Administration, 2019). Furthermore, the United States currently has 65 operating pressurized water reactors (PWRs) (the U.S. Nuclear Regulatory Commission, 2019). These statistics and the current administration's enthusiasm to dominate the world in nuclear power advancements (the U.S. Department of Energy, 2018) provided the main driving force behind this study.

1.4. Outline of Thesis

Figure 4 shows the overview of the content within this study. The 1/7 scaled reference spacer grid design taken from Navarro et al. (2011) is taken as the control

study. This reference spacer with the boundary conditions and fluid properties taken from the same study was used to establish a baseline and compare the results between the software package used in previous studies and ANSYS Fluent. Discrepancies in the results were looked at and the discussed. Mesh independent study was also conducted at the same time. Lastly, the various changes to the spacer grid design were put into the same fluid domain with the same working fluid properties and boundary conditions to find the geometrical factors with the most potential in improving the thermal cycle efficiency of a PWR power plant.

Under spacer grid lengths, this study simulated scaled lengths of 30 mm, 35 mm, and 40 mm. These chosen lengths all fitted in the reference domain and the 25% variation in scale provided good points of data to determine the significance of impact associated with the change. For variations of mixing vane angle, this study investigated angles of 25-, 27.5-, and 30-degrees because they fell within 20% change in magnitude from the reference.

Lastly, two variations with only slight changes to the manufacturing processes of spacer grids were investigated. A chamfer was added at the front of the spacer grid to lower the initial obliqueness of the spacer grid subchannels. This can be done by simple cutting or abrasive manufacturing processes to the spacer grid without specialized tooling. Additionally, a mixing vane with an inherit curvature in the construction was added to ease the transition of fluid back into the fluid domain outside of the spacer grid with the expected goal of lowering the amount of stagnation in the flow. The curvature may be added by simply changing the profile of the die used to press and stamp the mixing vane into the spacer during manufacturing. Again, these designs were chosen to

not over-complicate the construction, and therefore, the manufacturing, of the spacer grids.
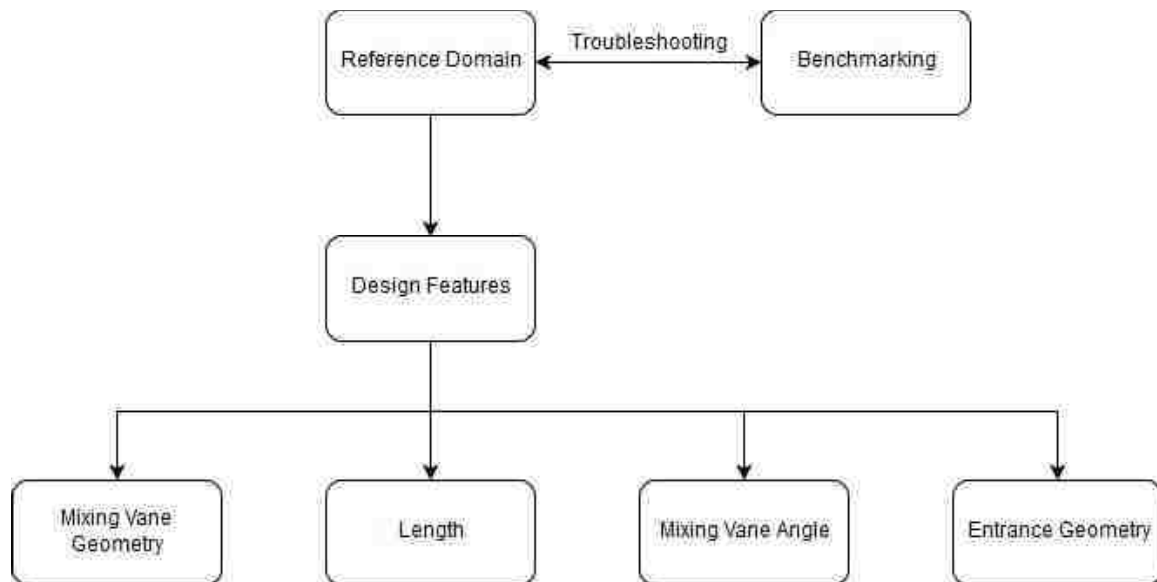
Figure 4 Flowchart of study content

CHAPTER 2 PROBLEM AND GEOMETRY

2.1. Problem Description

Excess pressure drops in fluid pressure across the reactor produces extra, unwanted, loads on the pump, reducing the power plant's thermal efficiency. Lowering the pressure drop caused by the reactor fuel rod spacer grids, decreases the unwanted loads. With the goal of increasing thermal efficiency in mind, lowering the unwanted loads become a necessity. However, manufacturing and supply chains of spacer grids are already in place and not flexible, so massive changes in design may not happen without significant changes and investments. Therefore, investigating the effects on simple variations on spacer grids already being produced can lead to changes that have significant improvements in hydraulic performance and light on investment.

Fortunately, the current spacer grids mainly consist of sheet metal stamped into form. This allows a few features such as bend angle or length to be altered without significantly altering the construction or adding to the cost. In other words, the current design, although not fully studied, has a lot of potential to improve without changing the method of construction and supply chain. So, altering the existing designs for improved hydraulic performance provides ways to optimize the spacer grid further without significantly changing the supply chain or requiring massive amounts of time and capital.

2.2. Geometry

This study used the sectioning method from Conner et al. (2010) and Navarro et al. (2011) to conserve the limited computational resources present. The domain was therefore separated into two halves according to the same strategy in sectioning the

11

domain provided by Navarro et al. (2011). Figure 5a shows the first half of the domain, which provides some length to the overall geometry prior to the fluid entering the spacer grid, in order to develop a velocity profile. The second half of the domain (section B), as shown in Figure 5a through Figure 5d, consists of the same arrangements of reactor fuel rods and a spacer grid. Figure 5 shows the arrangement of the two domains in relation to each other and the dimensions of the spacer grid inside of the second half of the domain (section B). Section A and section B of the domains were 100 mm and 60 mm, respectively. Moreover, Figure 5b specifically shows the mixing vane geometry from the side and front views.

Taken from the study done by Navarro et al. (2011), the spacer grid tested does not contain springs for computational simplicity. The pitch distance is 12.70 mm and the thickness is 0.48 mm., which represents a 1/7 scale of the actual spacer. The 5 x 5 grid also has an overall width of 49.13 mm. The overall length of the spacer grid without mixing vanes was 40 mm, as shown in Figure 5c. These parameters, when combined with a bare reaction rod of 9.5301 mm in diameter, results in a hydraulic diameter of 10.94 mm as shown in Figure 5d. The mixing vane contains an angle of 25-degrees, with 10 mm in depth, were set in a diagonal-offset pattern, as shown in Figure 5c,Figure 5d,Figure 6, andFigure 7.

The fluid domains (the negative space surrounding the spacer) were first created in SolidWorks 2017 Professional, then saved as a parasolid (".x_t") for importation into ANSYS Workbench. Figure 8 shows an overview of the domain creation process. Using a solid file format, such as parasolid; instead of a collection of surfaces, such as ".iges," allows the model editor in Fluent to recognize face of the solid as a continuous entity,

12

without the need to stitch the gap between imperfect surfaces together. Additionally, creating groups of surfaces into a "named selection" allows easier transfer of meshing and boundary condition settings between different fluid domains, since Fluent may apply the same settings to all the named selection with the same name.
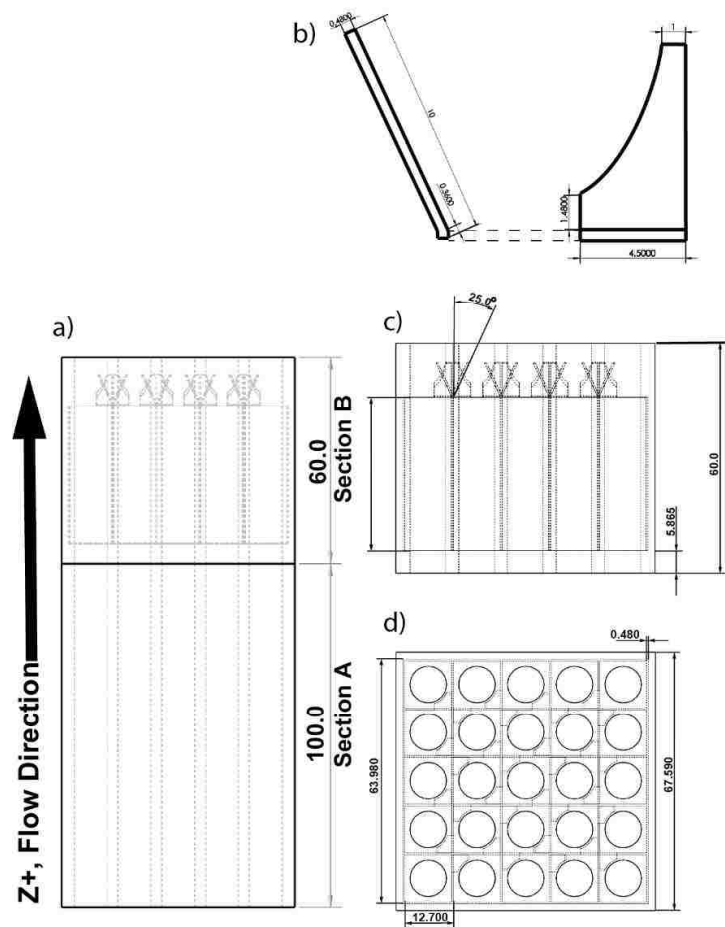
Figure 5 Reference spacer geometry used for control study, units in degrees and mm
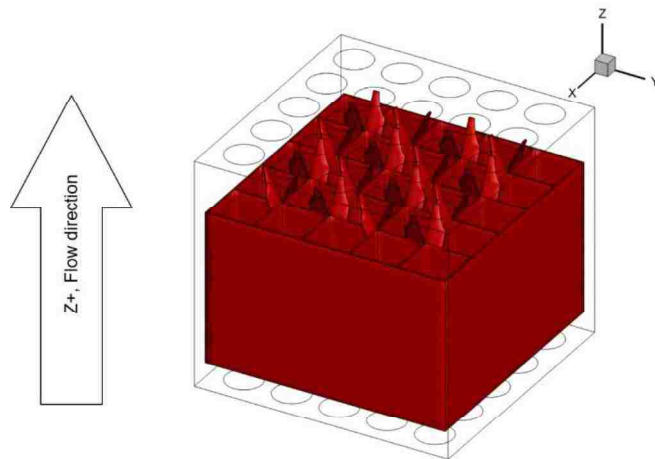
Figure 6 A section of the fluid domain simulated, with the spacer grid highlighted in red
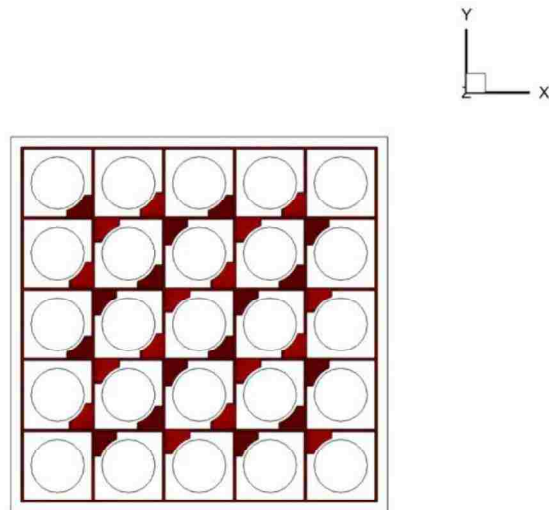
Figure 7 Top-view of the same section of the fluid domain in Figure 6, with the spacer highlighted in red

Figure 8 Converting geometry to computational domain

CHAPTER 3 NUMERICAL MODELLING AND METHOD VALIDATION

3.1. Numerical Methods

3.1.1. Fluid Modeling

The present study utilized incompressible fluid model for pressurized water, the primary working fluid in a PWR. This is because pressurized water has densities that are mostly constant, which simplifies the fluid modeling. As such, the following derivations of equations for an incompressible fluid were used to model the basic fluid behaviors in the domains covered in the present study. The governing equations for continuity and momentum below serves as the starting point:

$$\frac{\partial \rho}{\partial t} + \frac{\partial}{\partial x_j}\left[\rho \overline{u_j}\right] = 0 \tag{2a}$$

$$\frac{\partial}{\partial t}(\rho \overline{u_i}) + \frac{\partial}{\partial x_j}\left[\rho \overline{u_j u_i} + p\delta_{ij} - \tau_{ij}\right] = 0, i = 1, 2, 3 \tag{2b}$$

Equations $(2a)$ and $(2b)$ are the continuity and momentum equations of a fluid system, respectively. Additionally, since the scope of the present study only encompassed steady-state flow, the terms $\frac{\partial \rho}{\partial t}$ and $\frac{\partial}{\partial t}(\rho u_i)$ were set to zero. In simpler terms, flow is assumed to be in a steady state because the reactor has been running or operating for a while, with no change in density or momentum over time. Also, ideal incompressible fluids, such as compressed water should have a constant density, ρ.

Equations $(3a)$ to $(3f)$ depict the realizable $k - \varepsilon$ turbulence model used in the present study. This enclosure technique and the associated numerical model was used to generate reasonably accurate results within limited computational time and resources (Conner et al, (2010) and Liu et al, (2012)). The enclosure technique helps "enclose" the turbulent problem caused by the requirement for time-averaged values in order to solve the turbulence terms. These turbulent terms also create more unknowns than the amount of equations present, making analytical solutions difficult to obtain. Section 3.1.3 further describes this problem.

$$\frac{\partial}{\partial t}(\rho k) + \frac{\partial}{\partial x_j}(\rho k \overline{u_j}) = \frac{\partial}{\partial x_j}\left[\left(\mu + \frac{\mu_t}{\sigma_k}\right)\frac{\partial k}{\partial x_j}\right] + P_k + P_b - \rho \varepsilon - Y_M + S_k \tag{3a}$$

$$\frac{\partial}{\partial t}(\rho \varepsilon) + \frac{\partial}{\partial x_j}(\rho \varepsilon \overline{u_j}) = \frac{\partial}{\partial x_j}\left[\left(\mu + \frac{\mu_t}{\sigma_\varepsilon}\right)\frac{\partial \varepsilon}{\partial x_j}\right] + \rho C_1 S_\varepsilon - \rho C_2 \frac{\varepsilon^2}{k + \sqrt{v\varepsilon}} + C_{1\varepsilon}\frac{\varepsilon}{k}C_{3\varepsilon}P_b + S_\varepsilon \tag{3b}$$

$$\mu_t = \rho C_\mu \frac{k^2}{\varepsilon} \tag{3c}$$

$$k = \frac{1}{2}(\overline{u'^2_i}) \tag{3d}$$

$$\varepsilon = v(\overline{\frac{\partial u'_i}{\partial x_k}\frac{\partial u'_i}{\partial x_k}}) \tag{3e}$$

$$P_k = -\rho \overline{u'_i u_j}'\frac{\partial u_j}{\partial x_i} \tag{3f}$$

Where, "k" represents the turbulent kinetic energy, and "ε" represents the dissipation rate. C_1 and C_2 are the adjustable constants. Viscosity is defined in Equation $(3c)$; and Equation $(3d)$ expresses the production of "k." Furthermore, for the realizable $k - \varepsilon$ turbulence model, C_μ is not constant, but a function of the flow field. Meanwhile, "S" represents the mean rate-of-strain tensor, defined in Equation (4):

16

$$S \equiv \sqrt{2S_{ij}S_{ij}} \tag{4}$$

3.1.2. Finite Volume Method (FVM)

ANSYS Fluent utilizes the cell-centered finite volume method (FVM). In other words, Fluent divides a given fluid domain into numerous cells, each with its own numerical data on fluid properties. These values are all stored within the center of the cell element. Again, starting with Equation (5), the continuity equation, where the generation term per unit time, per unit volume, is assumed to be zero:

$$\frac{\partial u}{\partial t} + \nabla \cdot f(u) = 0 \tag{5}$$

which results in "u" being a conserved quantity. Additionally, re-writing $f(u)$ as a flux vector, of the quantity "u" from Equation (5), gives rise to Equation (6):

$$f(u) = [f_1(u), \dots, f_d(u)] \tag{6}$$

Then, using divergence theorem to integrate the flux, $f(u)$, from Equation (6) over a volume, V, within the domain, R^d (real domain), results a rewrite of Equation (5), in the form of Equation (7):

$$\frac{\partial}{\partial t} \int_V u dx + \oint_{\partial s} f_i n_i ds = 0 \tag{7}$$

where, ds represents the differential surface over the volume V, and $(n_1, \dots, n_d)$ represents the unit normal vectors pointing outwards of the surface ds. Next, the fluid

17

domain, V_h, is divided into cells that do not overlap in volume, but share surfaces with adjacent cells, V_r, which take on polygonal or polyhedral shapes. Equation (8) provides a mathematical expression of the controlled cell volume, V_r, and the complete fluid domain, V_h, expressed as the collection of all V_r's.

$$V_r, r = 1, \dots, N; \quad V_h = \bigcup_r V_r \tag{8}$$

Now, the average value of the quantity "u", u_r, over the cell volume, V_r, can be calculated as the integral of "u", as a function of the coordinates over the domain V_r, divided over the absolute volume of V_r, in Equation (9):

$$u_r = \frac{1}{|V_r|} \int_{V_r} u(x) dx \tag{9}$$

This quantity can represent any number of properties, such as velocity. Here, the above quantity represents momentum, which is conserved for every cell volume. Then, collecting the cells sharing a common face with the controlled cell V_r, forms the collection V_s, in Equation (10):

$$V_s = \{Set\ of\ cells\ which\ share\ a\ common\ face\ with\ V_r\} \tag{10}$$

Meanwhile, the law of conservation still hold true for the quantity, u_r, over V_r. This results in Equation (7) to be re-written into Equation (11). This is done by replacing the terms $\frac{\partial}{\partial t}\int_V u dx$ and $\oint_{\partial V} f_i n_i ds$ in Equation (7), with $|V_r|\frac{du_r}{dt}$ and $\sum_{s \in N(r)} \int_{V_r \cap V_s} f_i n_i ds$, respectively; using Equation (9) and Equation (10), respectively:

$$|V_r|\frac{du_r}{dt} + \sum_{s \in N(r)} \int_{V_r \cap V_s} f_i n_i ds = 0 \tag{11}$$

18

where, the second part of the equation represents the sum of all the fluxes of the quantity, u_r, over every surface the volume, V_r, shared with its adjacent cells.

It then remains to estimate the fluxes over the faces which V_r shares with its neighboring cells. Using Gaussian quadrature, with "p" Gaussian points, Equation (12) can be obtained as the following:

$$\int_{V_r \cap V_s} f_i n_i ds = \Delta s_{rs} \sum_{m=1}^{p} \omega_m F_{rs}^m \tag{12}$$

where, "ω_m" represents the Gaussian weights of the surfaces and F represents the approximated value of $f_i n_i$.

Monitoring the flux equation for each cell volume while simultaneously solving the governing equations provides the basis of FVM numerical fluid modeling.
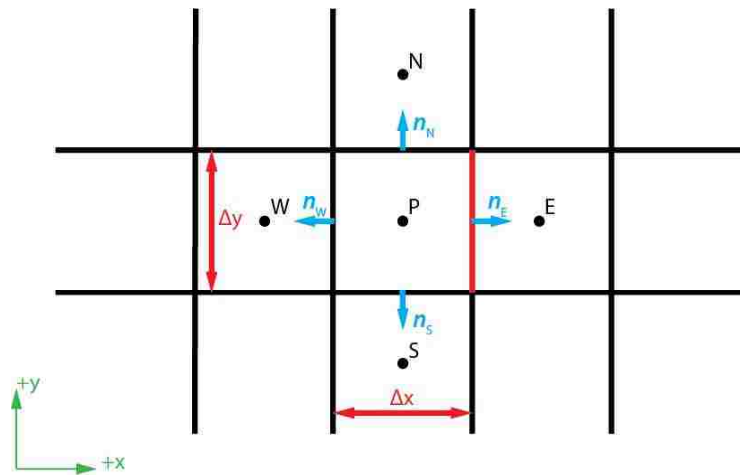

Figure 9 Simple 2-D representation of FVM

As shown in Figure 9 above, when the shaded control volume (CV) transfers a quantity, "u," to its neighboring volume "E," the quantity "u" will be weighed over the contact area S_n. In other words, the flux created by the quantity "u," taken at the cell

19

center, "P," which results in the vector field "n," will be integrated over the controlled surface "S_n," to determine the quantity of "u" transferred from the shaded CV to its neighboring cell, E.

3.1.3. Notes on ANSYS Fluent

ANSYS Fluent utilizes the Reynolds Average Navier-Stoke's (RANS) equation, Equation (13), to solve for the numerical solutions to the governing equations mentioned above. This is because of the parameters within the equations give rise to turbulent terms, which generates more unknown variables than the number of equations derived to provide an analytical solution. Equation (13) relies on multiple time-averaged values and closure techniques to be solved.

$$\rho \overline{u_j} \frac{\partial \overline{u_i}}{\partial x_j} = \rho \overline{f_i} + \frac{\partial}{\partial x_j} [-\overline{p} \delta_{ij} + \mu \left(\frac{\partial \overline{u_i}}{\partial x_j} + \frac{\partial \overline{u_j}}{\partial x_i} \right) - \rho \overline{u_i' u_j'}] \qquad (13)$$

This study uses the $k - \varepsilon$ turbulence model to solve the equation and its derivations. However, due to the above mentioned nature of the problem having more unknown than the number of equations, it must be solved numerically. This means various values were plugged in to both sides of the equation until the equation is balanced. In other words, the difference of the two sides must approach zero as a solution is reached. Then, the difference between the left side value and the right side value is called "residual." As a result, closely monitoring the value of the residual shows how "close" or "accurate" the current solution to the model is. Conversely, the lower the residual, the more accurate the result, and the longer it takes to compute the solution.

To reiterate, Fluent utilizes a cell-centered scheme for numerical computation. The method stores data at the center of each cell volume. Conversely, the flux vector used to calculate the solution in FVM requires the value at the boundary of a cell volume; therefore, the upwind scheme is developed in order to solve this issue.

3.1.4. Derivation of the Upwind Scheme

The upwind scheme was developed to eliminate the error caused by utilizing data points stored at the center of a cell to calculate values at the boundary. Consider, Figure 10, a simple, one-dimensional, cell arrangement:

Flow Direction
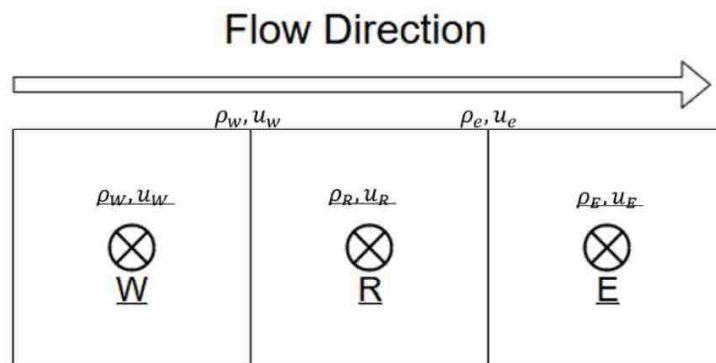
Figure 10 1-D Upwind cell diagram

where, the values ρ_W, u_W; ρ_R, u_R; and ρ_R, u_R, are stored at the cell-centers $\underline{W}$, $\underline{R}$, and $\underline{E}$, respectively. Meanwhile, the values ρ_w, u_w; and ρ_e, u_e are the correct values at the cell boundaries between cells $\underline{W}$ and $\underline{R}$; and $\underline{R}$ and $\underline{E}$, respectively.

Now, consider a steady-state convection-diffusion equation for momentum with no source term, as written in Equation (14). When applied to Figure 10, the continuity equation in the X-direction can be written in the form of Equation (15). After discretizing Equation (14) according to Figure 10, and applying Equation (15), the left-hand-side of

21

Equation (16) can be written. After substituting the convection mass flux terms, $(\rho u A)$, with F, the right-hand-side of Equation (16) can also be written.

$$\nabla \cdot \left(\rho \vec{V}\vec{V}\right) = -\nabla p + \mu \nabla^2 \vec{V} \tag{14}$$

$$(\rho u A u)_e - (\rho u A u)_w = 0 \tag{15}$$

$$(\rho u A)_e^i u_e^{i+1} - (\rho u A)_w^i u_w^{i+1} = F_e^i u_e^{i+1} - F_w^i u_w^{i+1} \tag{16}$$

Notice how Equation (16) demands the velocity data stored at the boundaries, specifically, u_e and u_w. However, the data that stored by the cell-centered scheme was from the center of the node, specifically u_E and u_W. One way to solve this error was to interpolate the data by using the data store at the next cell-center, which results in Equation (17).

$$u_e = \frac{u_R + u_E}{2}, u_w = \frac{u_W + u_R}{2} \tag{17}$$

Unfortunately, Equation (17) considers the contribution of the value from the next cell center in the current calculation. This is not ideal since the upwind cell, W in the case of Figure 10's flow direction, should be the only one with influence over the value at the boundary. As such, Equation (17) does not satisfy the transportiveness of the flow direction. As a result, using purely the upwind value, Equation (16) is now correctly re-written as Equation (18).

$$F_e^i u_e^{i+1} - F_w^i u_w^{i+1} = \begin{cases} F_e^i u_R - F_w^i u_W, & for \quad u > 0 \\ F_e^i u_E - F_w^i u_R, & for \quad u < 0 \end{cases} \tag{18}$$

Discretizing the right-hand-side of the Equation (14) yields Equations (19a) and (19b):

$$F_e^i u_R - F_w^i u_W = -\left(\frac{p_E - p_W}{\Delta x}\right) A \Delta x + \frac{\mu A_E}{\Delta x}(u_E - u_R) - \frac{\mu A_W}{\Delta x}(u_R - u_W) \qquad (19a)$$

$$F_e^i u_E - F_w^i u_R = -\left(\frac{p_W - p_E}{\Delta x}\right) A \Delta x + \frac{\mu A_E}{\Delta x}(u_E - u_R) - \frac{\mu A_W}{\Delta x}(u_R - u_W) \qquad (19b)$$

which may now be solved numerically, while minimizing the error of storing data at the cell centers. Meanwhile, 2nd order Taylor expansion was performed to Equations (19a) and (19b) to enhance accuracy by taking into account of the higher order terms.

3.2. Neglecting Gravity

The equations in Section 3.1 neglected the gravitational body force term in the modeling. This is due to the fact that the scaled computational fluid domain was scaled down to a small size highly insensitive to the impact of gravitational force. Figure 11 shows the effect of an added gravitational acceleration of $9.81 \frac{m}{s^2}$ on pressure, when applied to the reference spacer grid. The results were very close to the simulation without gravitational force. The resulting pressure drop with the inclusion of gravity was 12.2145 kPa, compared to a pressure drop of 12.4687 kPa when gravity was neglected, which amounts to barely 2.0% difference. This small amount of difference was not enough to justify the extra computational time since the computational resources was limited.
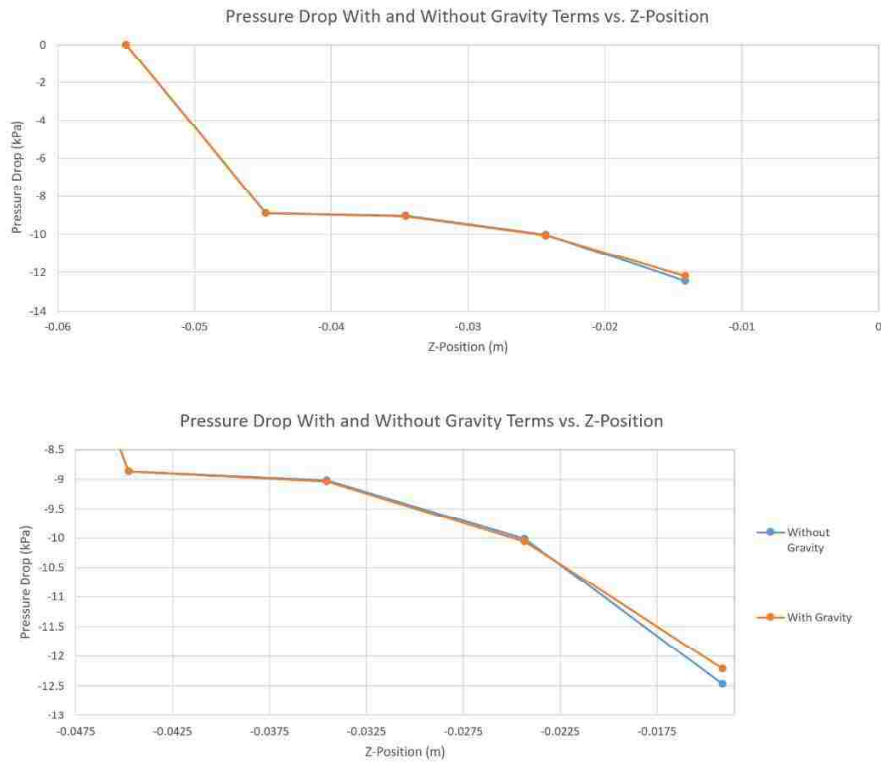
Figure 11 The pressure drop results from both the addition and the lack of gravitational pull upon the reference spacer grid (bottom: difference still barely discernable after zooming in)

3.3. Computational Domain Description

As previously mentioned, two sections of fluid domain exist in this simulation, section A and B, both using water as the working fluid. Due to the lack of energy equation and the exclusion of heat transfer, the temperature from Karouta et al. (1995) of $26.67°C$ was taken, yielding a density of $996.78\frac{kg}{m^3}$, and a dynamic viscosity of $8.572 \times 10^{-4}\frac{kg}{m-s}$. These fluid properties, when combined with the geometry as described in Section 2.2 and the boundary conditions describe in Section 3.4, yielded a Reynolds number of 8.64×10^4.

3.4. Boundary Conditions

The following boundary conditions were set:

- Section A has a constant inlet velocity of 6.79 m/s, with a reference gauge pressure of 483000 Pa, and a pressure outlet set at 0 Pa relative pressure. The resulting velocity profile at the outlet was exported.

- Section B has the exported velocity profile from section A set as the inlet, with a pressure outlet of 0 Pa. No-slip condition was also set on the walls and the spacer grid.

- Walls along the fluid domain include the no-slip condition.

3.5. Computational Meshing

In order to capture the boundary layer flow, the region where velocity distribution is dominated by shear stresses, the computational mesh sizing close to a non-moving walls needs to be smaller. This stems from the fact that in the viscosity-dominated region, the velocity distribution is not linear in the direction that is perpendicular to the wall. The way to capture this distribution correctly is to apply a wall function equation to calculate the velocity profile between cells where a data point does not exist. ANSYS has extensive setting parameters for the correct application of the wall functions. This includes the creation of a mesh with small body size around the wall and gradually increase the body size as the cell location gets further away from the wall. The act of gradually increasing body sizing is called "inflation." The combined effect of a small first

layer and inflation allows more precise capturing of the velocity profile near the wall as the cell density gets higher in the viscosity-dominated region.

To measure the quality of near-wall cells, a dimensionless parameter, y+, was used. A y+ value close to unity signifies good mesh quality. To determine the y+ value for a particular mesh, the Reynolds number in the axial direction, Re_z, is calculated first from Equation (20a), since it determines the flow characteristic. Next, the drag coefficient, C_f, is calculated through Equation (20b) to help determine the shear stress acting on the cell element along the wall, τ_{wall}, using Equation (20c). With the shear stress calculated, the friction-affected velocity, $U_{friction}$, can be determined from Equation (20d). Lastly, the first layer thickness, Δs, is multiplied by the density, ρ, friction-affected velocity, U_{fric}, and divided by the dynamic viscosity, μ, to determine the y+ value in Equation (20e).

$$Re_z = \frac{\rho U_\infty L}{\mu} \tag{20a}$$

$$Cf = \frac{0.026}{Re_x^{\frac{1}{7}}} \tag{20b}$$

$$\tau_{wall} = \frac{Cf\rho U_\infty^2}{2} \tag{20c}$$

$$U_{fric} = \sqrt{\frac{\tau_{wall}}{\rho}} \tag{20d}$$

$$y^+ = \Delta s \frac{U_{fric}\rho}{\mu} \tag{20e}$$

The boundary layer was set at 10 layers, with a first layer height of 6×10^{-6} m, and an inflation rate of 1.4. This resulted in a y+ value of around 1.75, as shown in Figure 12. All these parameters fall within the requirements for enhanced wall treatment, which

26

includes a y+ value close to unity and less than 4; with 10 inflating cell layers (ANSYS, Inc., 2009). Interestingly, the orientation of the mixing vanes also resulted in an asymmetric distribution of y+ values when a slice was taken in the YZ-plane.

In accordance to results from the mesh independent study mentioned in Section 3.5, body sizing for the entire fluid domain was set at 3×10^{-4} m. Tetrahedral cell elements and unstructured mesh was used to create a mesh more adaptive to the various smaller gaps in the geometry of the fluid domain. The culmination of the settings, including the boundary layers, generated 22.1 million elements in section A, and 61.8 million elements in section B. Figure 13 shows the overview of the mesh from the top, where the darker region represents the boundary layers with finer, inflating, mesh. Figure 14 shows a zoomed-in view of a corner of the generated mesh, where the boundary layer exhibits the inflating growth in size as it is further displaced from wall into the non-viscosity-driven flow region. Figure 15 shows another corner, from the top, where the inflation of the boundary layer can be seen more clearly. A see-through view of the mesh, as shown in Figure 16, shows a perspective of the mesh taken from the inlet, where boundary layers are also observed on the mixing vanes, in addition to other solid geometries. Lastly, Figure 17 shows the mesh of the boundary layers, with the body elements hidden, throughout the domain, which consisted of structured mesh.
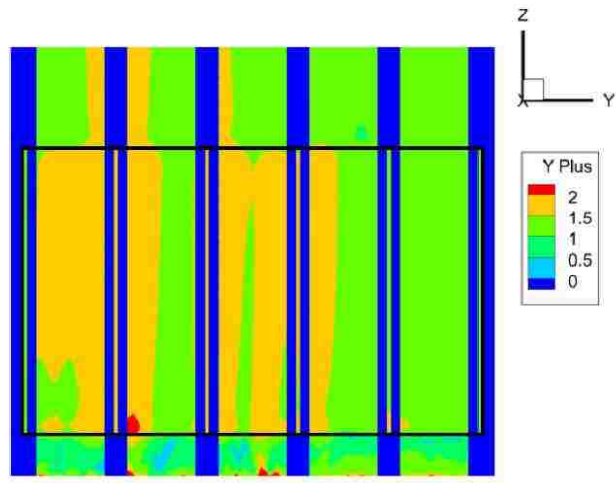
Figure 12 Y+ values within the domain; notice the values around the spacer grid (highlighted in black), with assymentric values near the outlet
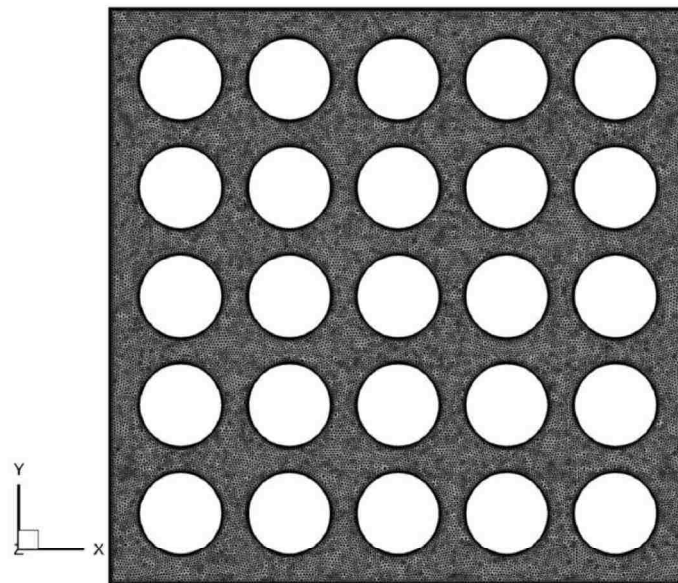

Figure 13 Top view of the mesh generated, showing the overall mesh, with the inflated boundary layers
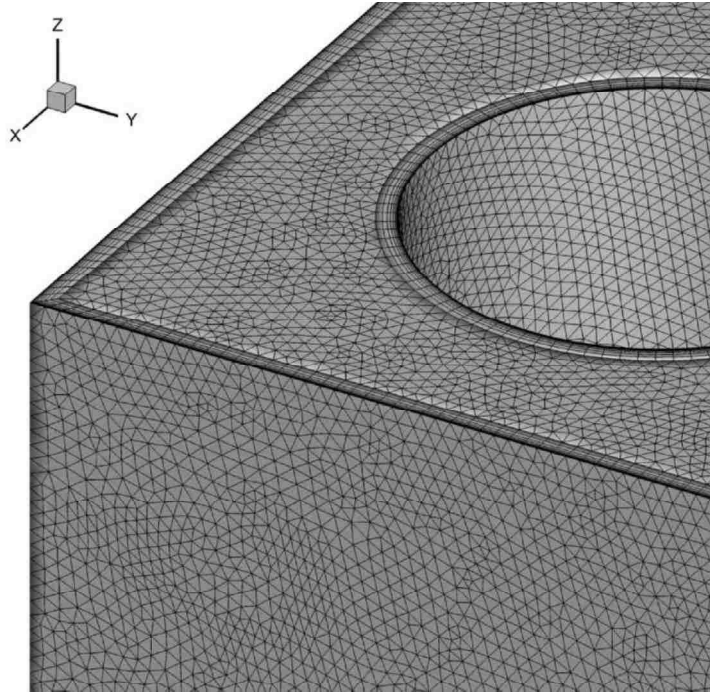
28

Figure 14 An isometric shaded corner view of the generated mesh, showing the boundary layers in 3-D (notice the lack of boundary layers in the y-z plane, which is a wall)
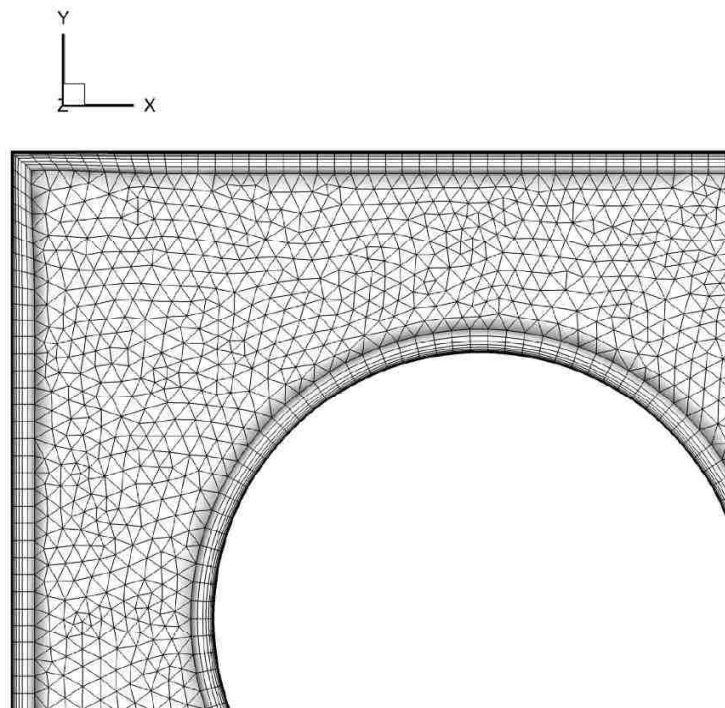

Figure 15 A top shaded view showing the boundary layers' structured mesh versus the unstructured mesh within the domain
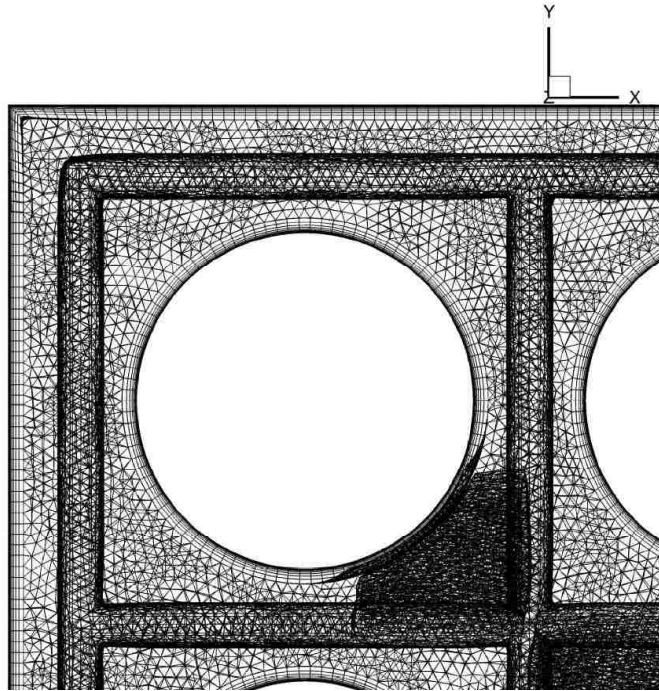
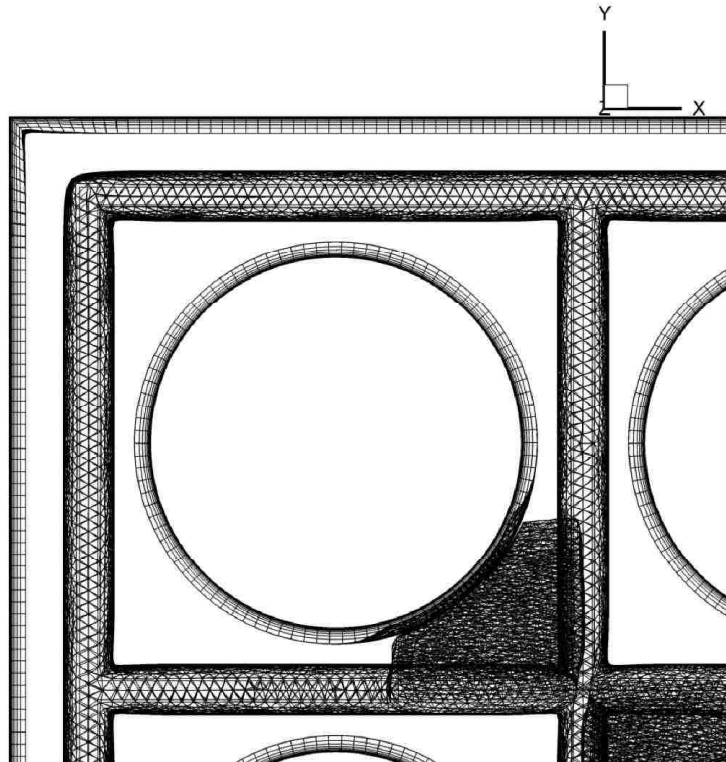**Figure 16 A top, see-through, view showing the boundary layers' structured mesh and the unstructured mesh within the domain**

Figure 17 A top, see-through, view showing the boundary layers' structured mesh, with the unstructured mesh hidden

3.6. Mesh Independent Study

Due to the nature of the upwind scheme, Fluent has another drawback which is associated with the mesh sizing. Since the upwind scheme requires the velocity data at the boundary, which is calculated by the diffusion-conductance term $\frac{\mu A}{\Delta x}$, and the pressure gradient calculated as a function of volume, as shown in Equation (19a) and Equation (19b), the numerical results from the scheme may vary from different body sizing. Fortunately, as the body sizing becomes smaller, both and diffusion-conductance term and pressure gradient terms error also become smaller to a point where the body sizing no longer contribute much variation to the solution. The resulting solution obtained at such a body sizing is known to be "mesh independent." To establish the body sizing where mesh independent results are generated, the same fluid domain is numerically simulated with different body sizing. Afterwards, the results are compared and the point where the results stabilize in relation to body sizing is determined and mesh independent results are established at that point.

Section A of the fluid domain, consisting only of the reactor fuel rods and no spacer, was simulated first to establish a rough mesh independent body size, with the numerical results and their associated body sizing in meters shown in Figure 18 and Figure 19. As shown, the numerical solutions for both pressure and velocity stabilized when body sizing was around 1.0×10^{-3} m. However, using references from Toth et al. (2008) Navarro et al. (2011) concluded that a mesh element count of 8×10^{6} was sufficient, which corresponds to a body sizing of 5×10^{-4} m.

31

Section B of the domain was simulated to conduct mesh independent study next. After failing to reproduce mesh independent results at the aforementioned elements count, body sizing was decreased until mesh independent results were obtained. The graphs in Figure 20 show that when the element count is higher than 4.23×10^7, the numerical results for pressure change becomes minute and independent from mesh size. However, since the highest element count in this particular case (i.e. 6.18×10^7 elements) only takes about 10% more time to reach convergence, when compared to 4.23×10^7 elements, the element count 6.18×10^7 was chosen. This element count translated to a body-sizing of 3.0×10^{-4} m.
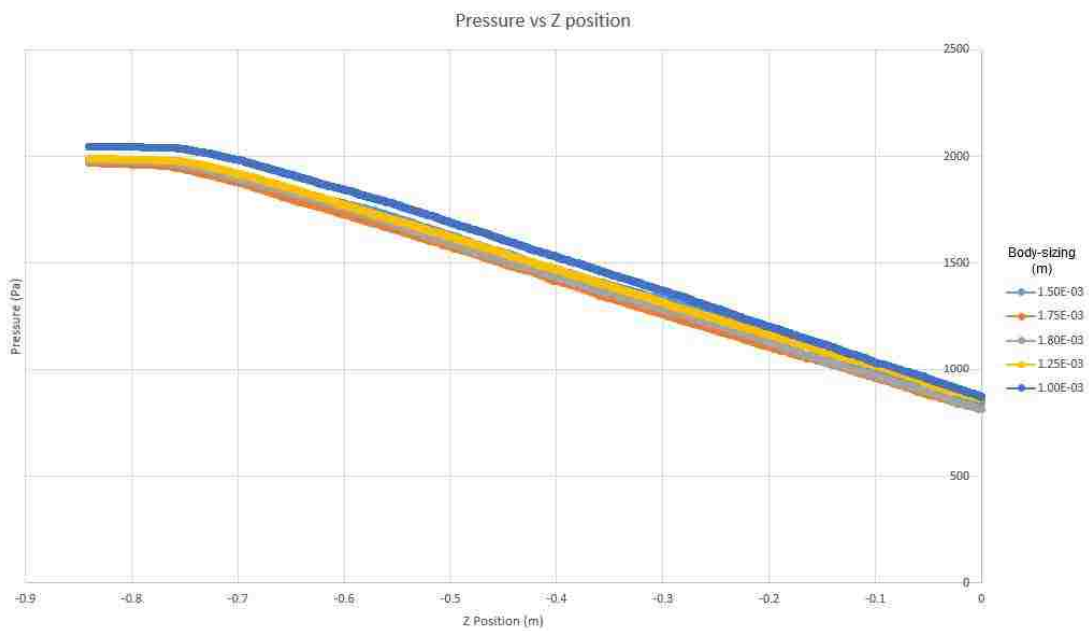

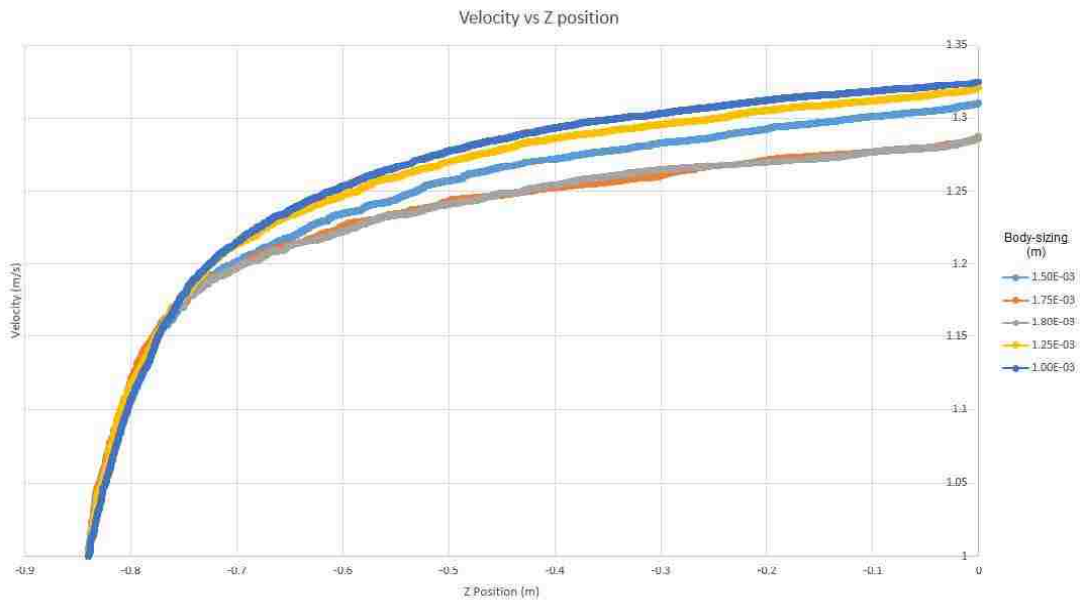**Figure 18 Bare rod mesh independent study pressure simulations**

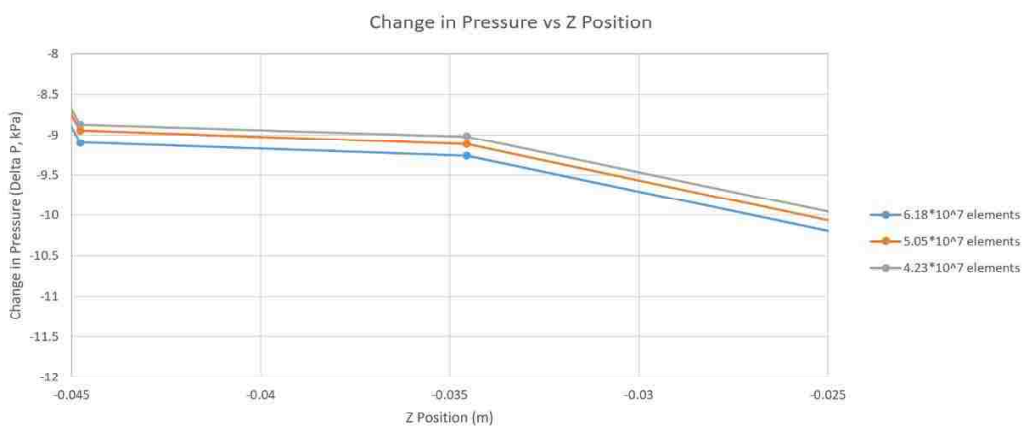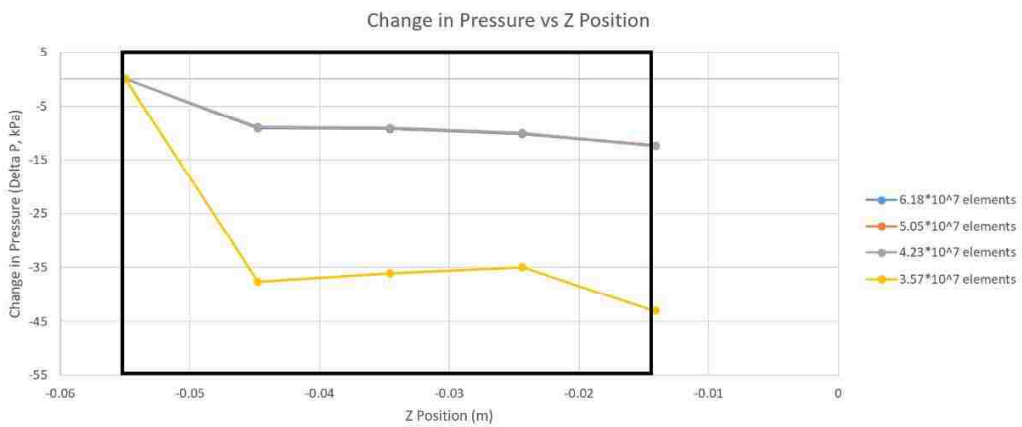**Figure 19 Bare rod mesh independent study velocity simulations**

Figure 20 Mesh independent study, with the spacer position highlighted in black; bottom graph zooms in to results from element counts higher than 4.23×10^7

3.6.1. Spacers Tested

As mentioned in previous sections, this study tested different variations of the spacer grids in 5 x 5 configurations. Three different grid lengths were tested, 40 mm, 35 mm, and 30 mm. Additionally, three different mixing vane angles were simulated as well, 25 degrees, 27.5 degrees, and 30 degrees. The objective was to investigate the pressure drop across the different configurations and compare these results with their respective agitation of the working fluid. Agitation was measured by dividing the magnitude of non-axial velocity over the magnitude of axial velocity at the outlet of section B domains.

Changing the length of the spacer grids help determine if running a higher number of shorter spacers produces more efficiency then running a lower number of longer spacers. Likewise, changing the mixing vane angle helps determine if increased agitation around the reactor fuel rod impacts the pressure drop across the mixing vanes.

The sectioning of the fluid domain pays dividends here as the bare fuel rod geometry in front of the spacer (section B) domain does not need to be re-evaluated for every single change in the spacer geometry. Flow does not need to be fully developed if velocity profiles were used as the boundary condition for section B of the domain, since calculations will continue from the obtained values. To make matters easier and have the calculations done on a manageable chunk of domain, the spacer domain required to be around 60 million elements. This worked out perfectly as the resulting element count for both domain sections converged within the target time of around a week.

3.7.Benchmarking

3.7.1. Pressure Drop Across Spacer Grid

To establish the accuracy of the present study, the numerical pressure solutions obtained here was compared to the previous data in pressure drop across the section B domain with the reference spacer grid geometry. Data sets compared included the semi-empirical Chun and Oh (1998), and the computational Navarro et al. (2011) and Karouta et al. (1995). Since most studies did not mention the X and Y location of where their data was taken, the present study elected to average the pressure across XY-planes at different Z (fluid flow direction) positions over the fluid domain. To accomplish this, the numerical results obtained from Fluent were exported as a Tecplot solution data file. These solution data files were imported into Tecplot 360, where data can be extracted from each XY-plane then averaged, using the integration tool. Figure 21 shows the pressure profile over the combined domain. Figure 22 shows that the pressure results at the interface between sections A and B is continuous, signifying the validity of the sectioning method. Figure 23 shows the extracted XY-plane data of the reference spacer grid, as seen in Tecplot 360.

Additionally, continuity residual, which indicates the numerical solution's satisfaction of conservation of mass, resulted in 3.3×10^{-7} for section A of the domain and 3.6×10^{-6} for section B. Figure 24 shows the data from the present study when compared to the data from previous studies. Although the overall pressure drop across the spacer grid in the present study was close to the previous results, the present study also included a dramatic pressure drop at the beginning of the spacer grid. Upon further investigation of the data point, it is noted that, beside the CFD study done by Karouta et

35

al. (1995), which did not take into consideration of spacer grid thickness, most studies lacked the data within the spacer geometry. The present study concluded that the likely suspect behind this phenomenon included boundary conditions, mesh size, resolution around the spacer which may fail to capture the developing boundary layer. Mesh size was ruled out since mesh independent study was conducted already and the results follow the general trend of previously done simulations and experiments, which is further discussed in Section 3.6.3. As for the developing boundary layers causing the dramatic pressure drop, it is clearly seen in the left hand side of Figure 25 where the dramatic pressure drop occurs when a slice of the domain was taken in the YZ-plane. When the left and right hand sides of Figure 25 are compared, it is clearly shown that the fluid flow undergoes sudden deceleration to enter the spacer, as pressure builds up around the entrance region of the spacer grid. Conversely, after the fluid entered the spacer, the developing boundary layer and acceleration of flow due to decreasing cross sectional area inside the spacer cause a drop in pressure around the tip of the spacer grid subchannels. This also explains the low pressure region around the surfaces perpendicular to the flow direction at the entrances of the spacer grid, caused by the large amount of drag from that particular surface. Since averaged pressure across different XY-planes were used for date points in the present study, the likelihood of taking data points strictly inside the boundary layer region was non-existent. Therefore, the reason should most likely to lie with the boundary condition. Specifically, whether the inlet boundary was too close to the spacer grid.
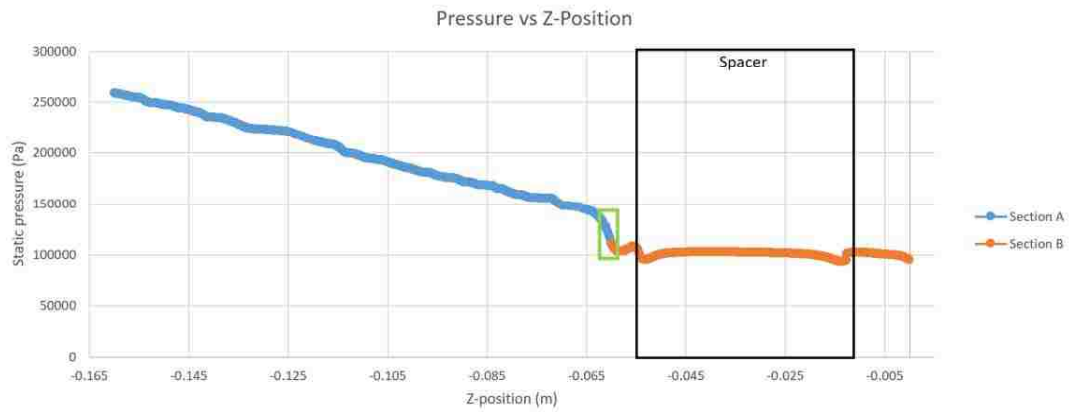
Figure 21 Pressure values across the combined domain, the interface between sections A and B is highlighted in green
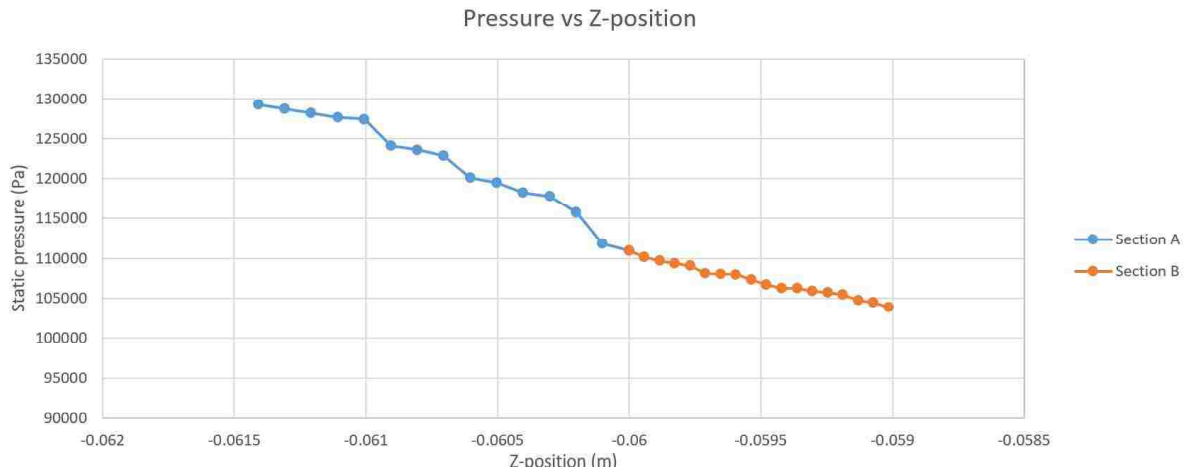

Figure 22 Pressure vales at the interface between sections A and B (green box in Figure 21)
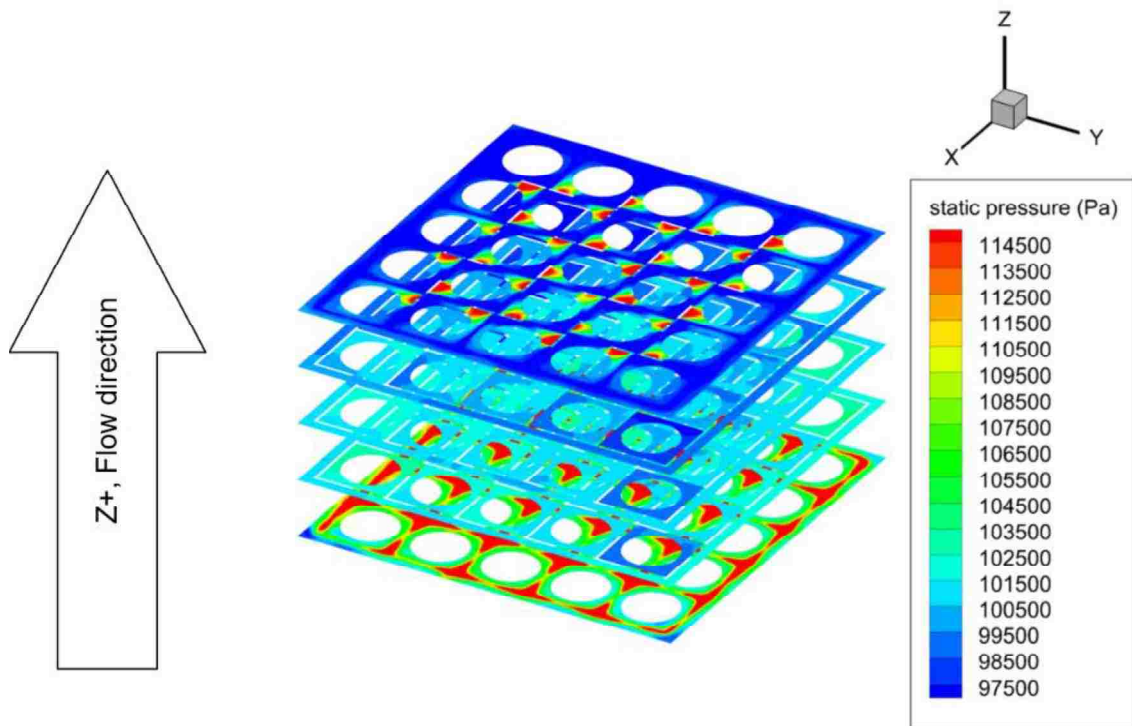
37

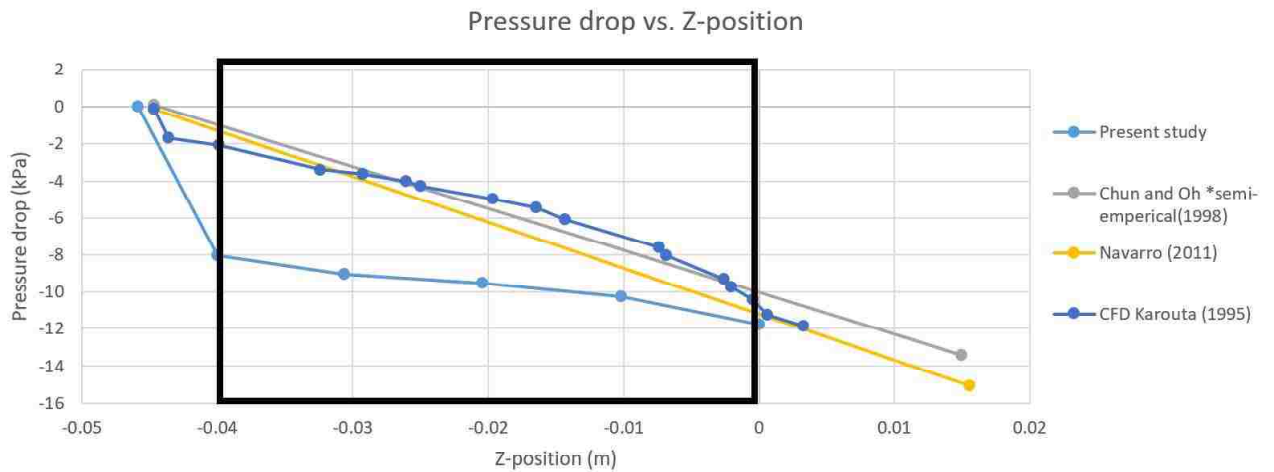**Figure 23 A 3-D isometric view of the slices of the domain where averaged pressure drops were taken**

Figure 24 Pressure drop across the domain, averaged over XY-planes at various Z-positions, compared to previous results in other studies, spacer grid location highlighted in black
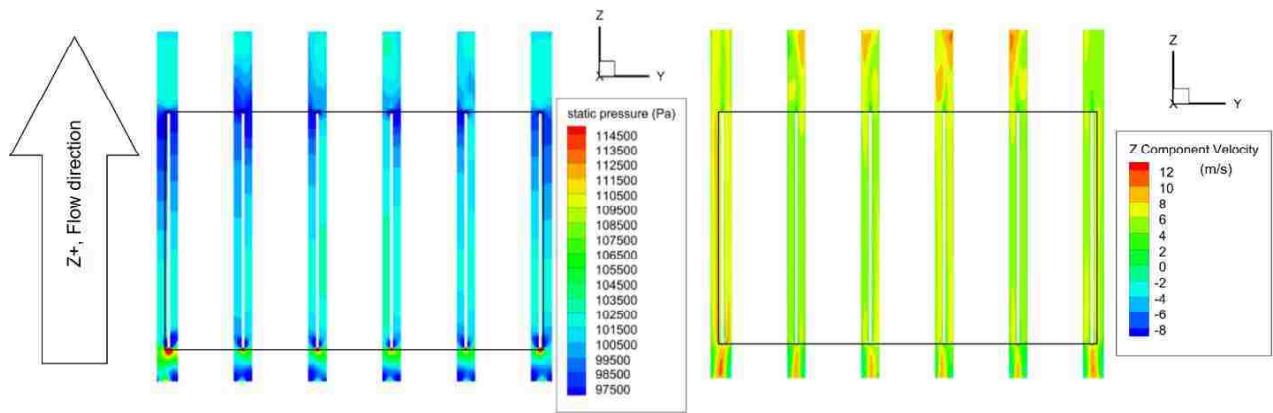
Figure 25 Pressure drop and velocity profiles in the middle YZ-plane, highlighted box denotes spacer location

3.7.2. Investigating Significant Spacer Grid Entrance Pressure Drop

In order to determine the validity of the hypothesis from Section 3.6.1, where it is assumed that the significant pressure drop across the spacer grid entrance was caused by the spacer grid's proximity to the inlet boundary condition, the distance between the inlet and the spacer grid entrance was lengthened and the new fluid domains simulated. Two different lengths, 19.05 mm and 37.658 mm, were added to the distance between the inlet and the spacer grid entrance in the section B domain. The resulting overall lengths of the domain tested in this section were 60 mm (reference), 79.05 mm, and 97.658 mm. Figure 26 shows the pressure drop results from these domains with overall lengths. Again observing Figure 26 shows that the working fluid did not reach a developed flow condition before entering the spacer grid in the reference computational domain. The increased pressure drop exhibited by the domain with longer overall length implies the above statement. Inherently, the pressure drop at the entrance stabilized at 79.05 mm

39

overall length, which also implies that fully developed flow can be reached if the

reference computational domain of section B was increased by 19.05 mm in the section

before the spacer.

Figure 26 Averaged pressure across different Z position slices over fluid domains with different total lengths, highlighted box denotes spacer location

CHAPTER 4 NUMERICAL MODEL RESULTS AND DISCUSSIONS

4.1. Results and Discussion

4.1.1. Lengths vs. Pressure Drops

Figure 27 shows the numerical results from the aforementioned spacer grid subchannel lengths of 40 mm (reference), 35 mm (i.e. -12.5%), and 30 mm (i.e. -25%). Figure 27 shows that total pressure drops across different spacer grid subchannel lengths showed minor differences since overall pressure drop was only reduced from 12.4287 kPa to 11.1659 kPa, a 10.2% difference, when the length of the spacer grid was reduced 25%. Spacer exit showed that longer spacer contributed to more pressure drop over the fluid region upstream of the mixing vane.
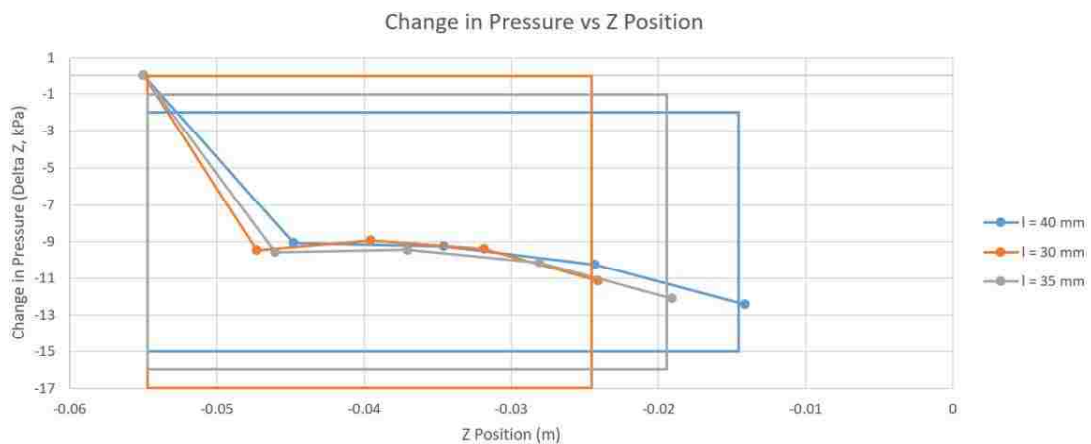

Figure 27 Change in average pressure across the various Z position slices with different spacer lengths, highlighted boxes denotes respective spacer location from the legend

4.1.2. Mixing vane angles vs. pressure drops

Figure 28 shows the difference with 20% increase in the mixing vane angle (25-to 30-degrees) resulted in a 0.84 kPa pressure loss, around a 9.28% increase. Interestingly,

the pressure increased after the mixing vanes as the fluid velocity decreased, due to the increasing cross sectional area, which induced a decrease in velocity. Also noticeable is the increase in drag force cause by the increase in mixing vane angle produces even less change in pressure drop when compared to the change in spacer grid length. The lack of dramatic impact on pressure drop showed great promise utilizing steeper mixing vane angles to increase agitation.
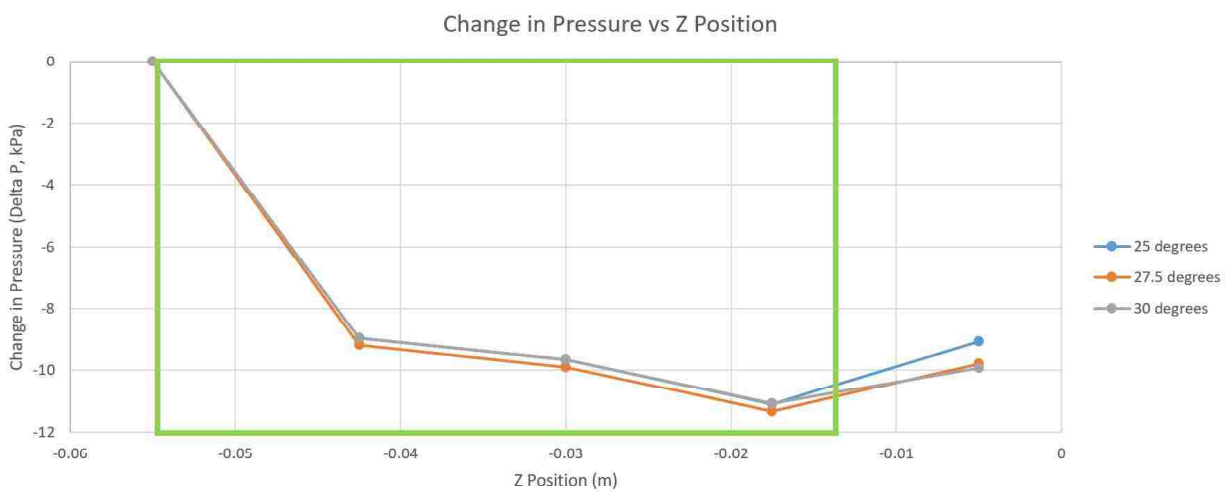

Figure 28 Different mixing vane angles slightly impact pressure drop by reducing different amounts of Z-velocity, highlighted green box denotes spacer location

4.1.3. Introduction to Swirl Factor

The primary reason behind changing the mixing vane angle lies with the increased agitation caused by the redirection of the fluid's velocity vectors. Mixing vanes with steeper angles redirect the fluid's velocity vector more due to the increase in turn angle applied to the fluid flow. When the fluid vector is redirected, the ratio between the axial and non-axial flow changes. Flow in the axial direction creates boundary layers due to the propagation of viscosity-driven flow in that direction. The two sections of boundary layers, thermal and hydraulic, both create detrimental effects on the heat transfer

performance of the reactor core. The hotter, slower, flow within these boundary layer region prevents the colder, faster, flow from directly interacting with the fuel rod elements to improve heat transfer rate. Increased non-axial flow velocities disturb these boundary layers, improving heat transfer from the reactor fuel rods elements to the working fluid. This agitation, or disturbance is measured by "swirl factor," (SF) a dimensionless measure of agitation, defined by the magnitude of the non-axial velocity over the magnitude of the axial velocity, which is discussed in Equation (21), below. As the its name suggests, a higher swirling factor means the fluid went under more agitation, resulting in the disturbance of thermal and hydraulic boundary layers, improving heat transfer.

$$SF = \frac{\sqrt{v_x{}^2 + v_y{}^2}}{|v_z|} \tag{21}$$

4.1.4. Mixing Vane Angles vs. Swirl Factor

As described in Section 4.1.2, increasing the mixing vane angles increases the swirl factors of that particular spacer grid. Additionally, also from Section 4.1.2, pressure drop does not increase significantly from the increase in the mixing vane angle. While the mixing vane angle was increased by 20%, the increase in pressure drop was around 9.28%. As shown in Figure 29, Figure 30, and Figure 31 this 20% increase in mixing vane angle improved the average SF by 0.0355, which was around 15.6% of the reference value seen in Figure 29. Figure 32 shows the axial velocity over the fluid domain with mixing vane angles, where the Z-direction velocity decreases as the mixing vane angle increases.
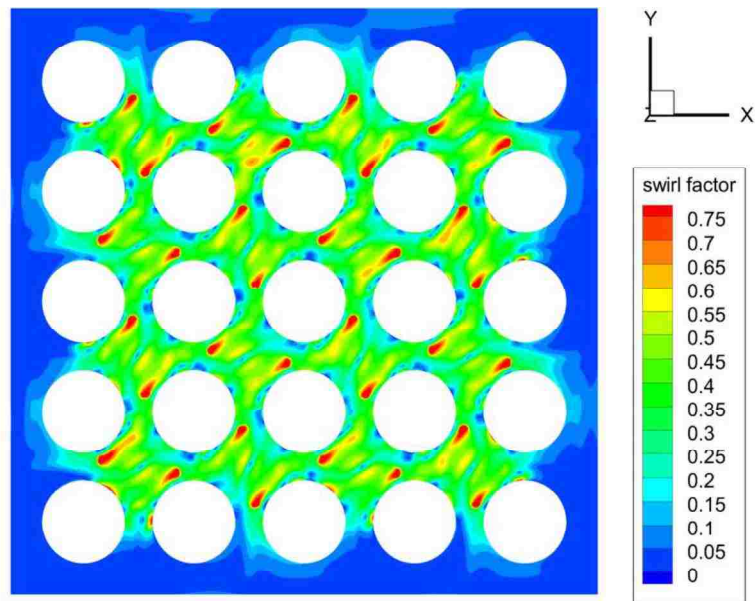
43

Figure 29 Swirl factor from 25.0-degrees of mixing vane angle, at a Z position slice taken at the end of the mixing vane (Z = -0.005 m), showing mixing vanes creating "wavy" circulating flows in the XY-planes, average value for SF was 0.228
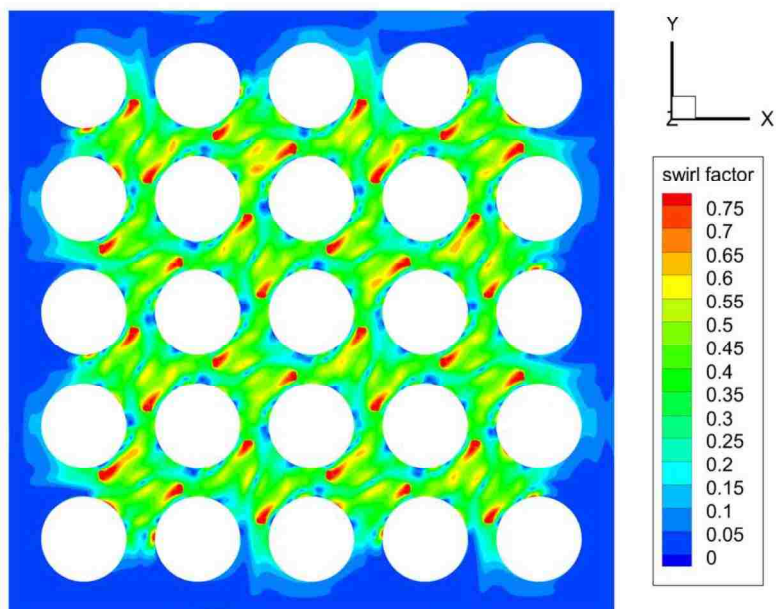

Figure 30 Swirl factor from 27.5-degrees of mixing vane angle, at a Z position slice taken at the end of the mixing vane (Z = -0.0051 m), average value for SF was around 0.263
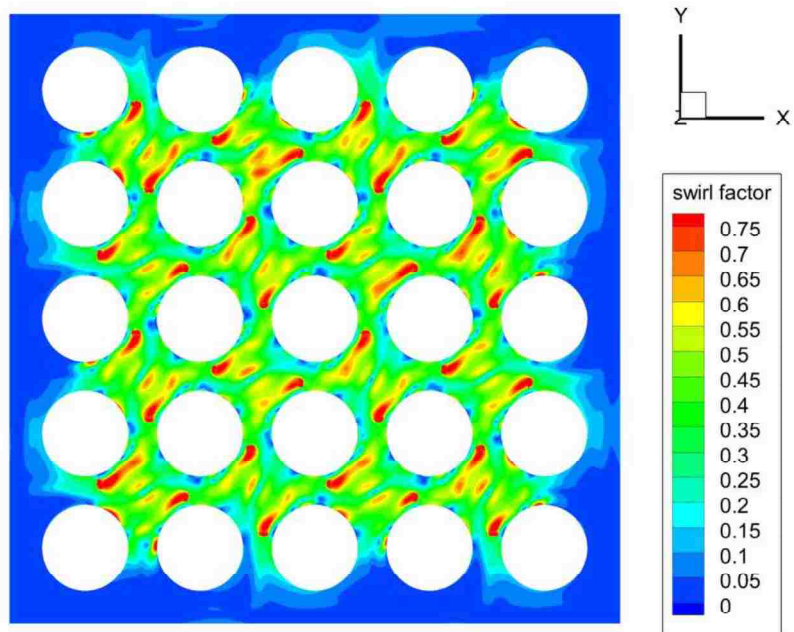
44

Figure 31 Swirl factor from 30.0-degrees of mixing vane angle, at a Z position slice taken at the end of the mixing vane (Z = -0.0055 m), average value for SF was a little over 0.263
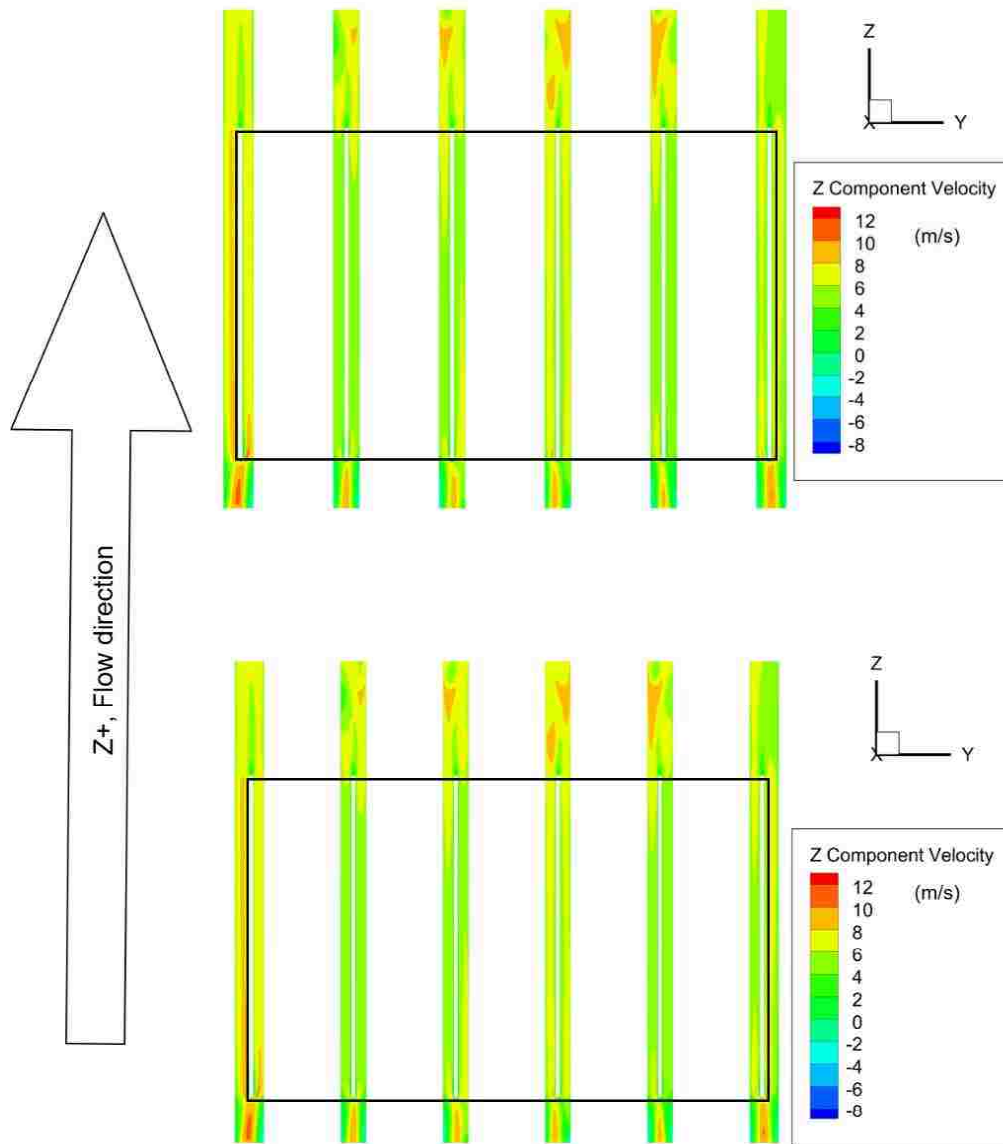
Figure 32 Velocity profiles at the middle YZ-plane resulting from changing mixing vane angles (top: 27.5-degrees; bottom: 30-degrees; highlighted boxes denote spacer location)

4.1.5. Effects of Chamfers on Reducing Entrance Pressure Drop

The significant pressure drop due to the perpendicular entrance geometry, as described in Section 3.6 inspired the addition of a 45-degree chamfer of depth 0.0075" at the entrance of the spacer grid. Figure 33 and Figure 34 show a 45-degree chamfer at the given depth bisects the thickness of the spacer grid, allowing the fluid to transition into the spacer grid without going through a geometry that is perpendicular to the flow direction, minimizing the enormous amount of drag. Figure 35 shows that with the added chamfer, the dramatic pressure drop at the entrance of the spacer grid decreased by a significant amount. The overall pressure drop also decreased from 12.4287 kPa to 6.5973 kPa, a change of 5.8314 kPa (i.e., 47% of reference value). Figure 36 shows the pressure and axial velocity distribution at the middle YZ-plane cross section of the fluid domain containing the spacer grid with the chamfer added. With the added chamfer, the domain exhibited a reduction of the pressure spikes at the entrance, while the velocity distribution was smoother and more even.
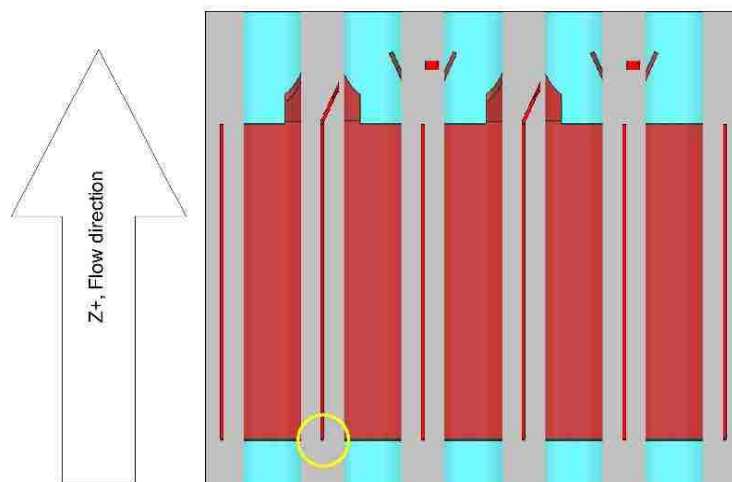

Figure 33 Spacer grid (highlighted in red) with 0.0075" of chamfer added to the front (circled in yellow), inlet-facing, side; gray represents the fluid domain, while blue represents the reactor fuel rods
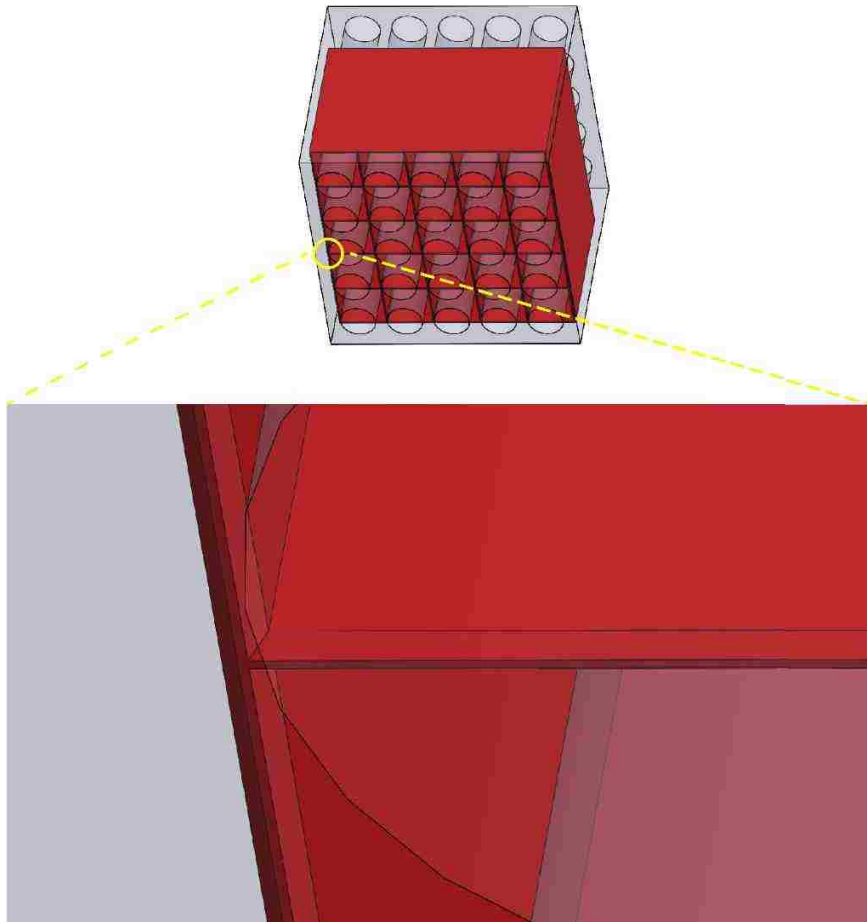
47

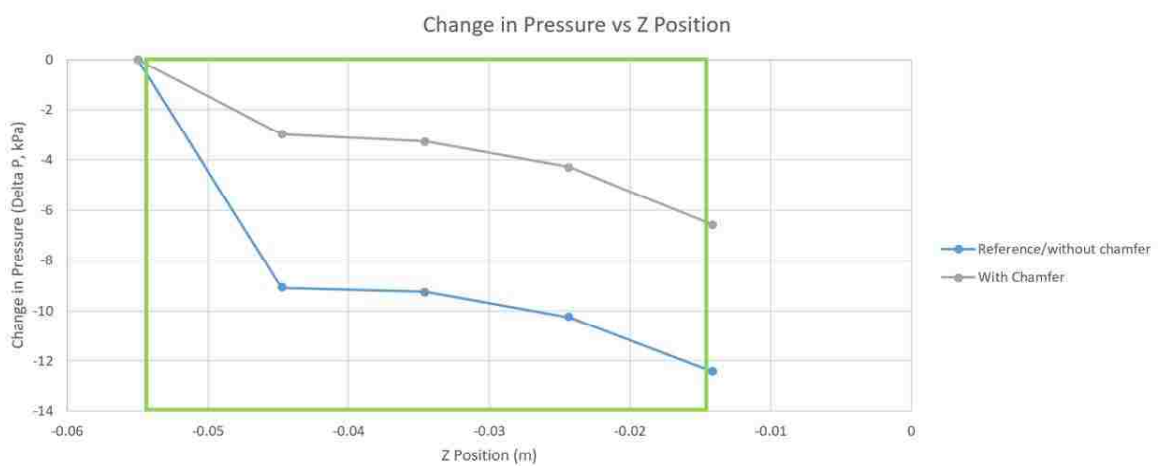**Figure 34 Bottom angled views of the spacer grid with chamfer added**

Figure 35 Pressure drop of the reference spacer versus the same spacer with chamfer added (spacer grid location highlighted in green)
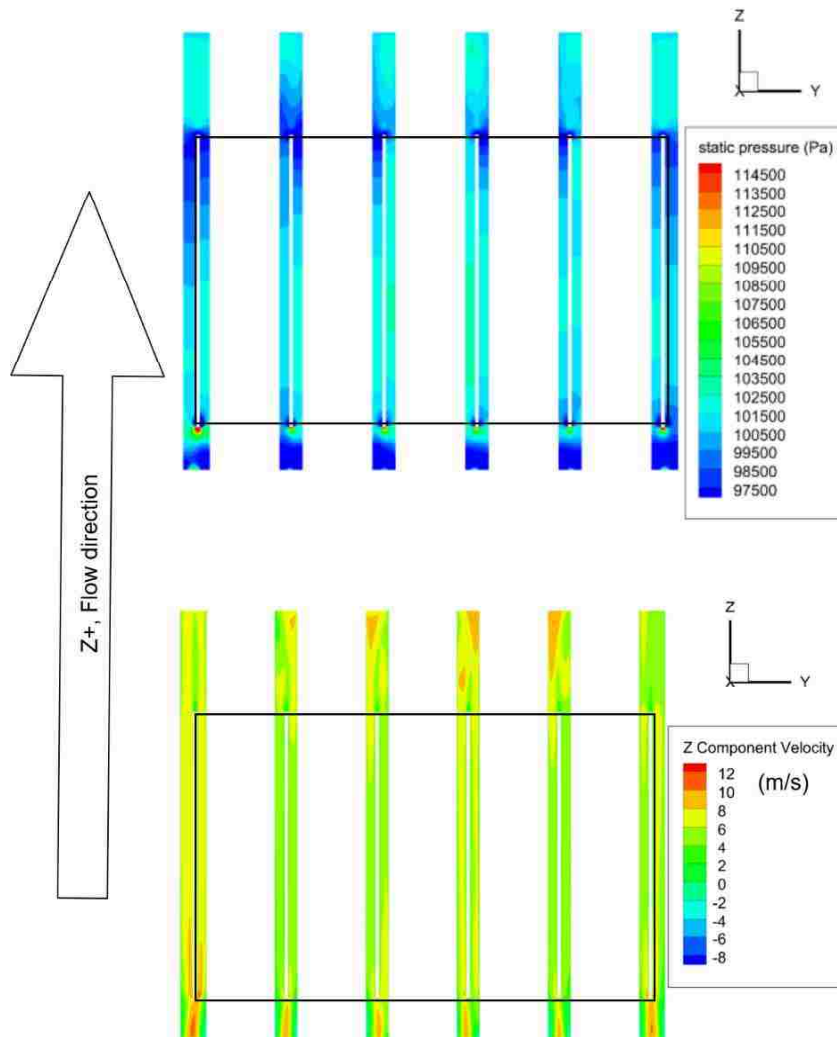
Figure 36 Pressure and Z-direction velocity distribution at the middle YZ-plane cross section of the spacer grid with added chamfer (top: static pressure; bottom: Z-direction velocity, highted boxes denote spacer location)

4.1.6. Spacer Grid with Curvature-added Mixing Vanes

Due to the success of adding chamfer to ease the flow transitioning into different geometric conditions, a curvature was added to the mixing vane of the reference spacer grid. In theory, the transition to a mixing vane geometry with a curvature should lessen the amount of stagnant flow downstream of the mixing vanes, due to the decreased and

49

less abrupt turn angle at the end of the curvature, when compared to a straight mixing vane, which in turn, should lessen the pressure drop. In order to keep the same blockage ratio and total cross sectional footprint when viewed axially, the constraints and dimensions shown in Figure 37 were applied to the curvature. This eliminated the change in results that may stem from other factures other than shape. The conclusion drawn from Figure 38 and Figure 39 is that the resulting fluid characteristics of the curvature-added mixing vane was poor. Adding the added curvature caused both an increase in pressure drop and a decrease in swirl factor. Figure 38 shows the pressure drop increased from 9.08056 kPa to 11.9422 kPa (i.e. 31.3%,), while Figure 39 shows the swirl-factor decreased from 0.228 to 0.218 (i.e. 4.3%). Velocity profile in Figure 40 shows the increased Z-direction velocity which caused the swirl-factor change.

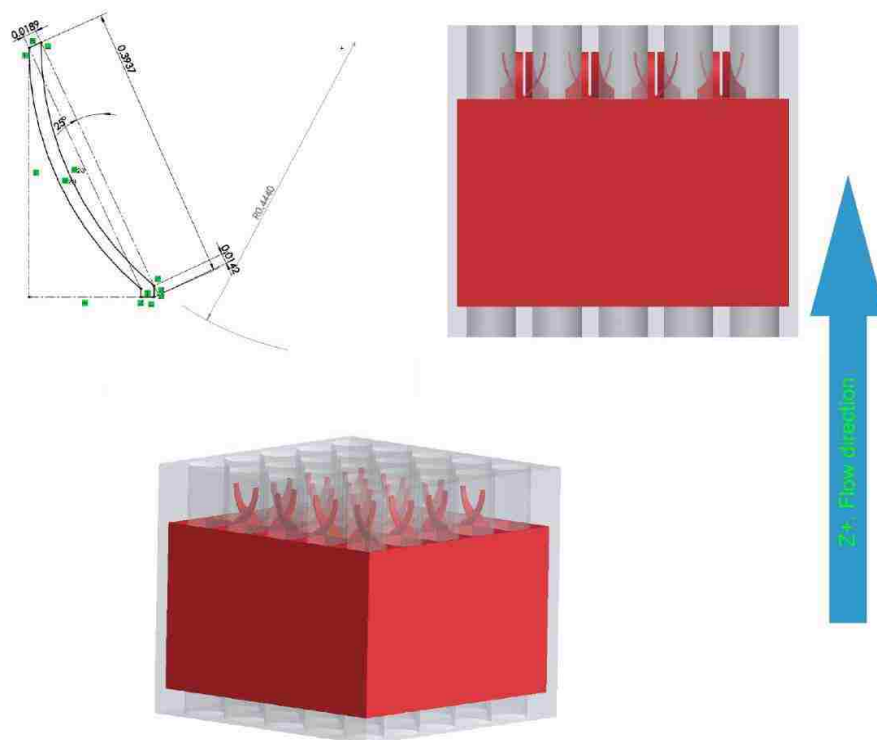**Figure 37 Spacer grid with a curvature added to the mixing vane**
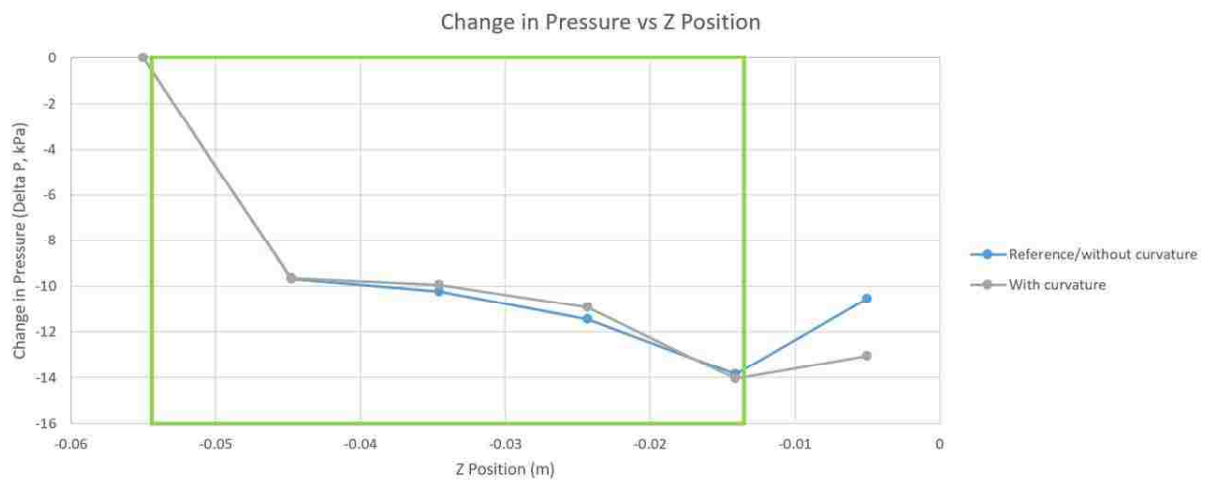
Figure 38 Pressure drop of the reference versus the curvature-added spacer grid (spacer grid location highlighted in green)
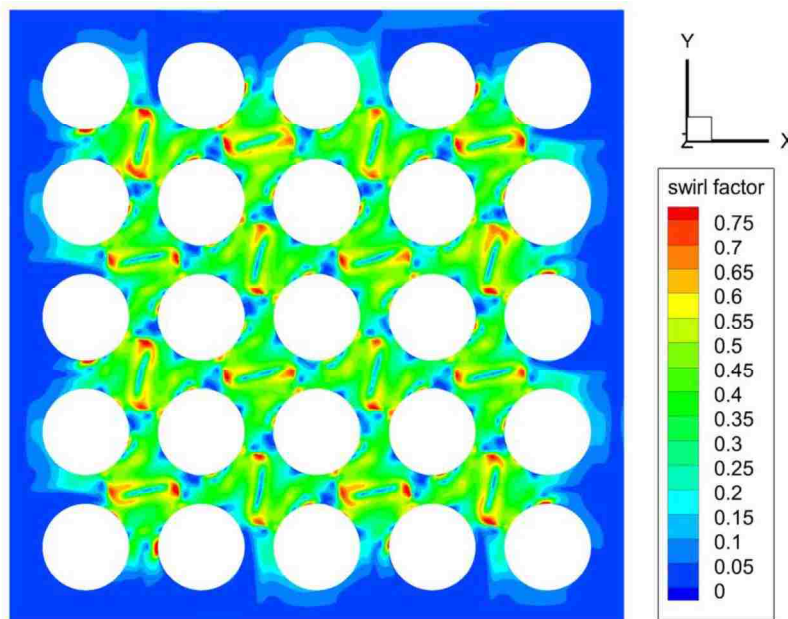

Figure 39 Swirl factor of the curvature-added mixing vanes, on an XY-plane at the Z-position where the mixing vanes end (Z = -0.005, same as reference due to applied geometrical constraints)
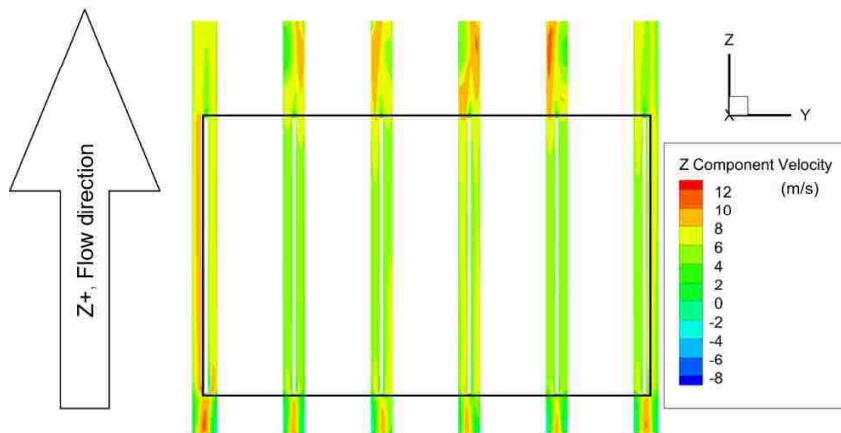
51

Figure 40 Velocity profile of the spacer grid with added curvature, at the middle YZ-plane, highlighted box denotes spacer location

CHAPTER 5 CONCLUSIONS AND FUTURE WORK

The results obtained in the present study indicated that increasing the mixing vane angle to increase the swirl factor does not significantly impact the pressure drop across the fluid domain. This provides a great way to increase agitation, and potentially, heat transfer within the reactor core, with relatively less increase in extra parasitic loads at the pump. However, in the case of increasing swirl-factor, axial velocity cannot drop too significantly so that the fluid become stagnant, resulting in the reactor fuel rods overheating.

On the other hand, changing the length of the spacer grid subchannels impacts the pressure drop more significantly. The added potential for extra vibration exhibiting in the reactor core due to the lessened amount of geometry holding the reactor fuel rod elements in place needs to be further investigated. Additionally, using more numerous spacer grids with shorter subchannels, may increase performance due to the increase in mixing vane count, too.

Likewise, lessening the subchannel pressure drop around the entrance region may also decrease the pressure drop dramatically with relatively low cost by the addition of a chamfer at the entrance of the spacer grid. The reduction of drag forces around the region should also increase stability of the bundles by reducing fluid-related vibrations and the size of the low pressure pockets.

Future work includes the addition of heat transfer, which involves changing the mixing vane angles to optimize swirl-factor/heat transfer while retaining enough axial velocity to prevent reactor core meltdowns. Potential projects also include the development of numerically correlated models for the spacer-length, chamfer

angle/depth, and mixing vane angle to help with future predictions and thus, the

optimization of simple spacer grid geometry.

REFERENCES

ANSYS, Inc. ANSYS FLUENT User's Guide. 2009
<http://www.afs.enea.it/project/neptunius/docs/fluent/html/ug/main_pre.htm> (Retrieved on 02/28/2019)

Chen, D., Xiao, Y., Xie, S., Yuan, D., Lang, X., Yang, Z., and Lu, Q. (2016). Thermal–hydraulic performance of a 5 × 5 rod bundle with spacer grid in a nuclear reactor. *Applied Thermal Engineering, 103*, 1416-1426. doi:10.1016/j.applthermaleng.2016.05.028

Cheng, Songbai and Chen, Huandong and Zhang, Xiaoying. (2016). CFD analysis of flow field in a 5 × 5 rod bundle with multi-grid. *Annals of Nuclear Energy. 99*. 10.1016/j.anucene.2016.09.053.

Conner, M. E., Baglietto, E., and Elmahdi, A. M. (2010). CFD methodology and validation for single-phase flow in PWR fuel assemblies. *Nuclear Engineering and Design, 240*(9), 2088-2095. doi:10.1016/j.nucengdes.2009.11.031

Chun, T., and Oh, D. (1998). A Pressure Drop Model for Spacer Grids with and without Flow Mixing Vanes. *Journal of Nuclear Science and Technology, 35*(7), 508-510. doi:10.3327/jnst.35.508

Ikeda, K., Makino, Y., and Hoshi, M. (2006). Single-phase CFD applicability for estimating fluid hot-spot locations in a 5×5 fuel rod bundle. *Nuclear Engineering and Design, 236*(11), 1149-1154. doi:10.1016/j.nucengdes.2005.11.006

Karouta, Z., GU, Chun-Yuan, and Schoelin, B. (1995). 3-D flow analyses for design of nuclear fuel spacer. In: Proceedings of the 7th International Meeting on Nuclear Reactor Thermal-hydraulics (NUREG/CP--0142-Vol4). New York, United States, pp. 3153-3174

Liu, C., Ferng, Y., and Shih, C. (2012). CFD evaluation of turbulence models for flow simulation of the fuel rod bundle with a spacer assembly. *Applied Thermal Engineering, 40*, 389-396. doi:10.1016/j.applthermaleng.2012.02.027

Office of Nuclear Energy, The, Untied States Department of Energy, The. Light Water Reactor Sustainability (LWRS) Program. 2019 <https://www.energy.gov/ne/nuclear-reactor-technologies/light-water-reactor-sustainability-lwrs-program> (Retrieved on 03/14/2019)

Navarro, M. A., and Santos, A. A. (2011). Evaluation of a numeric procedure for flow simulation of a 5 × 5 PWR rod bundle with a mixing vane spacer. *Progress in Nuclear Energy, 53*(8), 1190-1196. doi:10.1016/j.pnucene.2011.08.002

Rehme, K. (1973). Pressure Drop Correlations for Fuel Element Spacers. *Nuclear Technology, 17*(1), 15-23. doi:10.13182/nt73-a31250

Smith, L. D., Conner, M. E., Liu, B., Dzodzo, B., Paramonov, D. V., Beasley, D. E., . . . Holloway, M. V. (2002). Benchmarking Computational Fluid Dynamics for Application to PWR Fuel. *10th International Conference on Nuclear Engineering, Volume 3*. doi:10.1115/icone10-22475

Toth, S. Aszodi, A., 2008. CFD analysis of flow field in a triangular rod bundle. *Nuclear Engineering and Design*. doi:10.1016/j.nucengdes.2008.08.20.

United States Department of Energy, The. (2018, September 28). President Trump Signs Bill to Boost Advanced Nuclear in America. <https://www.energy.gov/articles/president-trump-signs-bill-boost-advanced-nuclear-america> (Retrieved on 03/14/2019)

United States Energy Information Administration, The. (2019, January 24). Annual Energy Outlook 2019. < https://www.eia.gov/outlooks/aeo/> (Retrieved on 03/14/2019)

United States Nuclear Regulatory Commission, The. (2019, January 23). List of Power Reactor Units. <https://www.nrc.gov/reactors/operating/list-power-reactor-units.html> (Retrieved: 03/15/2019)

Versteeg, H., and Malalasekera, W. (2007). *An Introduction to Computational Fluid Dynamics*. Harlow: Prentice Hall.

White, F. M. (2003). *Fluid mechanics*. Boston: McGraw-Hill.

White, F. M. (2006). *Viscous fluid flow*. New York: McGraw-Hill.

Yao, S and Hochreiter, and J. Leech, W. (1982). Heat-Transfer Augmentation in Rod Bundles Near Grid Spacers. *Journal of Heat Transfer-transactions of The Asme - J HEAT TRANSFER*. 104. 10.1115/1.3245071.

CURRICULUM VITAE

Wan Chuan Fan

Email Address: jasonfanjf@hotmail.com

Education

University of California, Davis
B.S., Biotechnology, September 2013

University of Nevada, Las Vegas
B.S., Mechanical Engineering, May 2018

Thesis Title

Numerical Study of Spacer Grid Geometry in a 5 x 5 Nuclear Fuel Rod Bundle

Examination Committee

Yi-Tung Chen, Ph.D., Examination Committee Chair
Professor, Department of Mechanical Engineering
University of Nevada, Las Vegas

Robert Boehm, Ph.D., P.E., Examination Committee Member
Professor, Department of Mechanical Engineering
University of Nevada, Las Vegas

William Culbreth, Ph.D., Examination Committee Member
Professor, Department of Mechanical Engineering
University of Nevada, Las Vegas

Jichun Li, Ph.D., Graduate College Representative
Professor, Department of Mathematics
University of Nevada, Las Vegas